Photoelectron Spectroscopy with Synchrotron Radiation

F. J. Himpsel

IBM Research Division, Thomas J. Watson Research Center

P.O. Box 218, Yorktown Heights, NY 10598

This article intends to give an overview of the capabilities of photoelectron spectroscopy in determining the electronic structure of bulk solids, thin films, and surfaces. Particular emphasis is placed on the use of synchrotron radiation as a tunable, polarized, and well-collimated light source. Current trends in the field are higlilighted, and examples from the author's recent experience are given.

I. Introduction and Outline

Photoelectron spectroscopy is arguably the most popular techI nique employed at today's ultraviolet and soft x-ray synchrotron radiation sources[1-4]. The reason for its popularity is the versatile nature of the photoemission process. It allows, on one hand, an in-depth look at all the quantum numbers of electronic states in a solid by using the energy, angular, polarization, and spin dependence of photoemission. On the other hand, it is possible to integrate over most of these parameters in core level spectroscopy and characterize the local bondin; around an atom by a single number, i.e. the core level binding energy, which has simple correlations with charge transfer and coordination.

In the following we will first give a brief overview of the instrumentation currently used, putting emphasis on methods for increasing efficiency by simultaneously detecting several variables, and by streamlining the sample turnaround. We will then proceed to valente and ccre level spectroscopy results, zooming in on selected areas, such as current trends in band mapping, "enginrered" solids, and semiconductor surface chernistry.

II. Instrumentation

II.1 Spectrometers

The key to an efficient photoelectron spectrometer has proven to be simultaneous detection of several variables. Most frequently, photoelectrons are counted over a whole spectrum of energies (typically 10^2 channels) by a position-seisitive detector in the dispersion plane of a hemispherical analyzer.[5] Such setups are standard in angle-resolved photoemission, combining efficiency with good argle and energy resolution. They can also be used in core level spectroscopy to obtain ultimate surface sensitivity by picking out grazing escape angles for the photoelectrons.

There have been successful attempts to detect more than one variable simultaneously, but the corresponding spectrometers are custom designs and have not become as easily available as the commercial hemispherical systems. Several types of toroidal analyzers[6] provide siinultaneous detection of the energy and one angle. Display spectrometers[7-9] detect two angles, making them well-suited for photoelectron diffraction and holography where one wants to look at a large number of escape e directions while keeping the photoelectron energy fixed. The number of image elements can be 10^2 x 10^2 = 10^4 pixels, speeding up the data collection enormously. Figure 1 shows an improved version of a design that has been used by several groups.[7] It turns out that display spectrometers operated in the angle-integrating mode exhibit the highest collection efficiency ("etendue") of all current spectrometer designs, making them well-suited for core level spectroscopy, too.

11.2 Spin Detectors

Spin detectors have always been a handicap for extending photoelectron spectroscopy to magnetic systems. Conventional Mott detectors had to accelerate the photoelectrons to 100 keV in order to measure the spin asymmetry in Mott scattering of the electrons at heavy nuclei (typically Au). The high energy made them bulky and the efficiency was only 10^{-4}. Due to clever design and lowering of the energy these detectors have come down in size, and their efficiency has increased. Another avenue (Fig. 2, Ref.[10]) uses the spin asymmetry in scattering at the electrons surrounding heavy nuclei (again typically Au). This can be done

at much lower energy (about 150eV), such that the spin detector can be attached to the rear end of a mobile, angle-resolving spectrometer. The main problem is to obtain an absolute calibration of the spin polarization (it cannot be calculated and changes over time) and a sensitivity to changes in the photon and electron beam geometry.
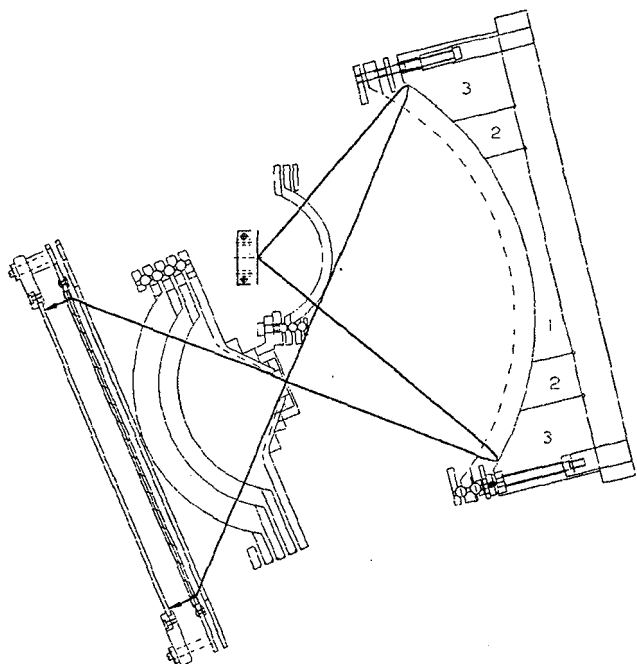

Figure 1: Display-type spectrometer[7] imaging the angular dependence of photoelectrons. The electron energy is selected by combining an ellipsoidal repelling mirror as low pass and a retarding grid as high pass. The mirror is divided into 5 sections with three slightly different potentials (1-3) in order to compensate for changes in the angle of incidence across the ellipsoid. Two extreme electron trajectories are shown, originating at the sample, and ending on a phosphor screen after amplification by a pair of channel plates.

11.3 Timing

The pulsed nature of synchrotron radiation suggests applications such as time-of-flight energy analysis and coincidence experiments. All this has been demonstrated, mostly in atomic physics where detection efficiency comes at a premium. However, many synchrotron sources have only very short intervals between pulses, or require a special, single bunch mode for timing applications. Therefore the use of the time structure has never really caught on in solid state spectroscopy. As an example of a recent application we mention coincidence spectroscopy between photoelectrons and Auger electrons.[11] It promises several interesting features, some of which have been demonstrated, e.g. reducing the core level lifetime broad-

ening, eliminating extrinsic secondary electron background, and probing the valence electronic structure of specific atoms, labelled by their core levels.
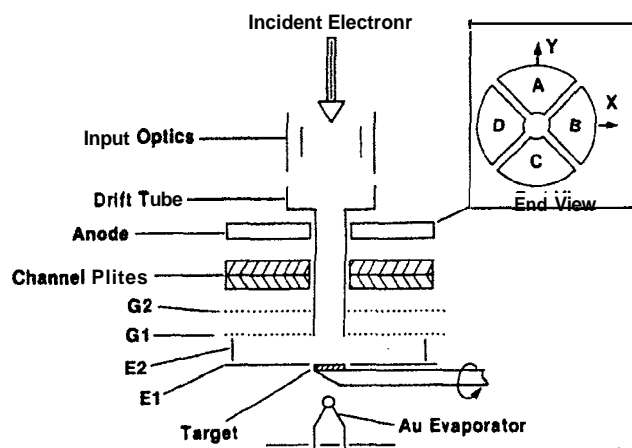

Figure 2: Spin detector[10] based on the asymmetry of the backscattering amplitude of low energy (150eV) electrons from a Au film.
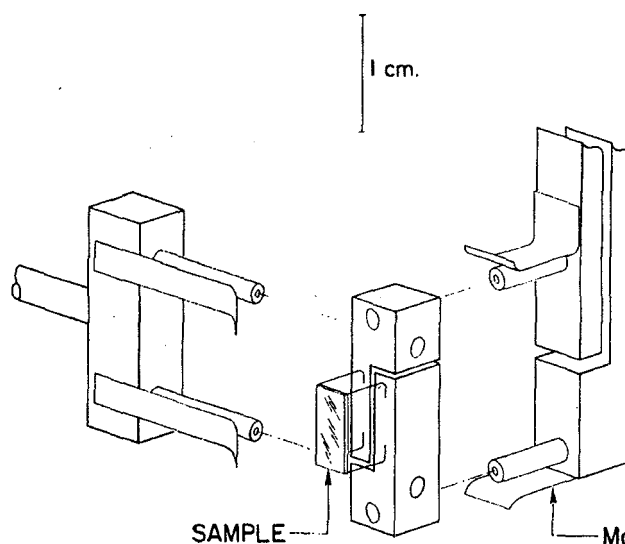

Figure 3: Sample transport mechanism using fork-like manipulators. The sample holder is split to be able to heat the sample resistively.

11.4 Efficient Sample Preparation

With today's high-powered synchrotron radiation sources the main bottleneck in data acquisition ceases to be the data taking time. Instead, sample preparation takes on this role, as the surface and thin film structures under study become ever more complex. This follows a general trend in surface science away from analyzing simple model surfaces and towards synthesizing novel structures. Therefore, the design of a photoelectron spectroscopy beam line has to take into account efficient introduction and preparation of samples,

preferably without breaking vacuum. Beyond that, the switching period from one user to another is becoming a significant fraction of the beam time, requiring new schemes for making the transition smoother or allowing for quick distribution of monochromatized photons between multiple end stations.

Various sample transfer systems have become popular that allow sample holders to be moved between a preparation chamber and the photoelectron spectrometer. In addition, an air interlock and a sample magazine allow for rapid introduction of new samples and extraction of samples that need fixing. Beyond that the author has found it quite useful to bring in small evaporators mounted on sample blocks. The most popular transfer systems are based on fork-like manipulators (Fig. 3) or bayonet locking mechanisms. The main drawback of sample transfer systems is the difficulty in cooling and in accurate temperature control.
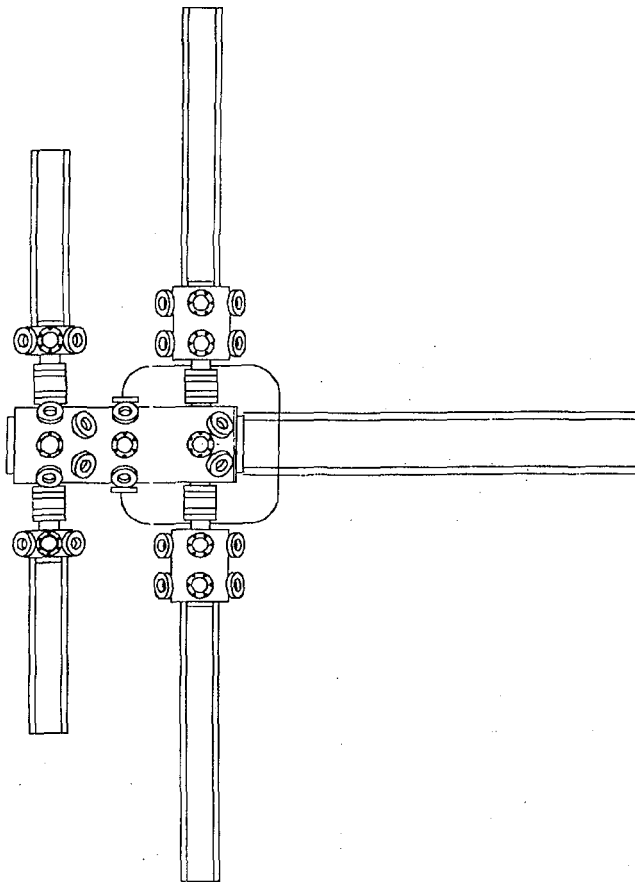

Figure 4: Arrangement of sample preparation chambers into a central analysis chamber and four satellite chambers using sample transfers via bellow manipulators. The satellite chambers can be used for independent sample preparation methods (cleaving, gas exposure, evaporation, introduction lock) to speed up the turnover.

At the nest higher level of integration (Fig. 4) it has proven to be very useful to attach a number of satel-

lite chambers to the preparation chamber via sample transfer through a valve, each of them equipped with a specific preparation technique, e.g. a certain evaporator, or a particular gas for chemical vapor deposition or chemical/ion etching. Thereby one minimizes cross-contamination between the preparation methods and can switch rapidly from one experiment to the other.

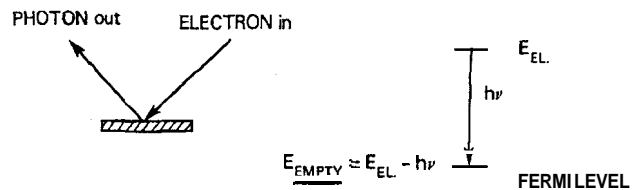**PHOTOEMISSION**
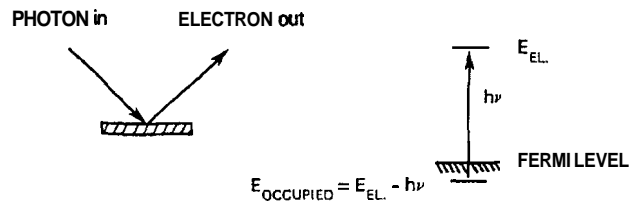
INVERSE PHOTOEMISSION

Figure 5: Schematic of photoemission and inverse photoemission as probes of occupied and empty states, respectively.

At the highest level of integration we are currently designing a switching system between several experimental stations, to be attached to an undulator beam line at the Advanced Light Source (ALS) at Berkeley. While switching with mirrors is feasible at photon energies up to about 100eV, the deflection angles become too small at higher energies to separate the experimental chambers sufficiently. Therefore, we have placed all experimental chambers on a platform that pivots around a point close to the exit slit of the monochromator, such that a simple rotation of the platform shifts the light from one experiment to the other.

III. Valence Band Spectroscopy

III.1 Band Mapping

The electronic structure of a solid is completely characterized by a set of quantum numbers. For a crystalline material these are energy E, momentum k,

point group symmetry (i.e., angular symmetry), and spin. This information can be summarized by plotting $E(\mathbf{k})$ band dispersions with the appropriate labels for point group symmetry and spin. Disordered solids (e.g. disordered alloys) can be characterized by average values of these quantities, with disorder introducing a broadening of the band dispersions. The experimental techniques that can probe all of the quantum numbers are photoemission,[3] and its time-reversed counterpart inverse photoemission[12] (Fig. 5). The former probes occupied states, the latter unoccupied.
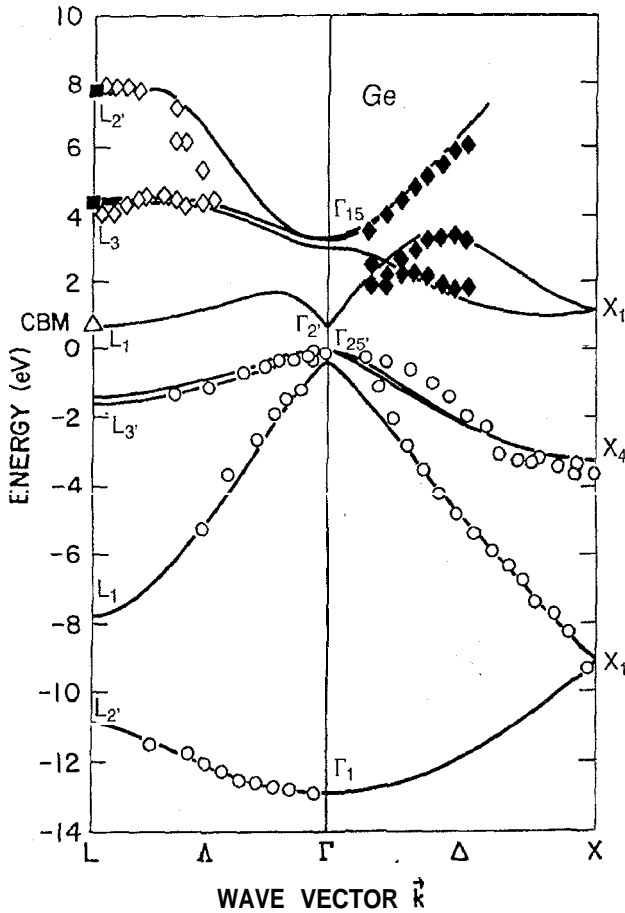

Figure 6: Band dispersions[13] of Ge from photoemission and inverse photoemission (symbols), compared to a first principles quasiparticle calculation (lines).

How are energy band dispersions determined? A first look at the task reveals that photoemission (and inverse photoemission) provides just the right number of independent measurable variables to establish a unique correspondence to the quantum numbers of an electron is a solid. The energy E is measured from the kinetic energy of the electron. The two momentum components parallel to the surface, $\mathbf{k}^{\parallel}$, are measured from the polar and azimuthal angles of the electron. The third

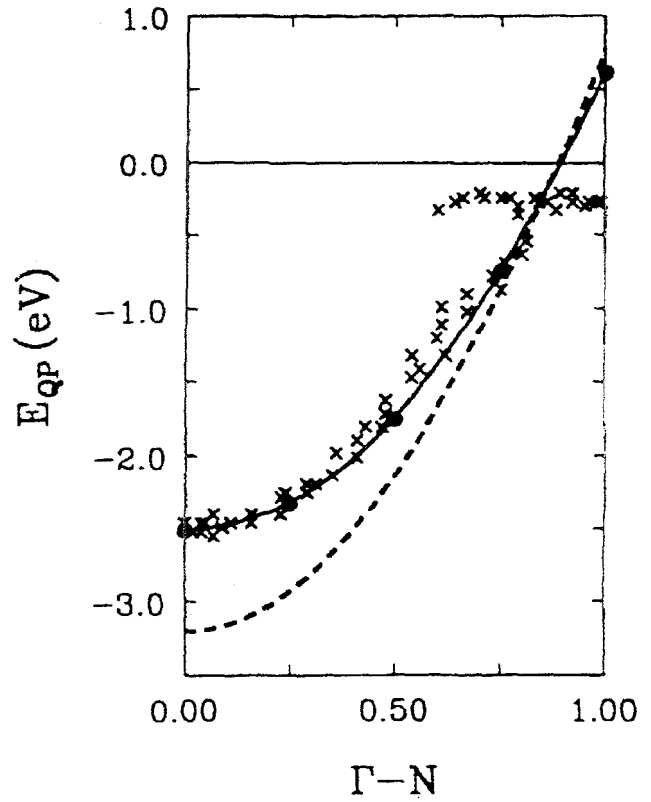
Figure 7: Band dispersion[14] of delocalized electrons in Na (symbols) compared to local density eigenvalues (dashed) and quasiparticle energies (full). The difference, i.e. the self-energy shrinks the band width.

momentum component, $k^{\perp}$, is determined by tuning the photon energy hv, thus requiring a tunable photon source (or a tunable photon detector in inverse photoemission) for a complete band structure determination. Finally, the spin-polarization of the electron provides the spin quantum number, and the polarization of the photon provides the point group symmetry.

For two-dimensional states (e.g., in layered crystals and at surfaces) the determination of energy bands is almost trivial since only E and $\mathbf{k}^{\parallel}$ - the momentum parallel to the surface - have to be determined. These quantities obey the conservation laws

$$E_{\ell} = E_{\mathbf{u}} - h\nu \qquad (1)$$

and

$$\mathbf{k}_{\ell}^{\parallel} = \mathbf{k_u}^{\parallel} - \mathbf{g}^{\parallel} \qquad (2)$$

where $\mathbf{g}^{\parallel}$ is a vector of the reciprocal surface lattice, u denotes the upper state and ℓ the lower state. These conservation laws can be derived from the invariance with respect to translation in time and in space (by a surface lattice vector). For the photon, only its energy hv appears in the balance because the momentum of an ultraviolet photon is negligible compared to the momentum of the crystal electrons. The subtraction of a
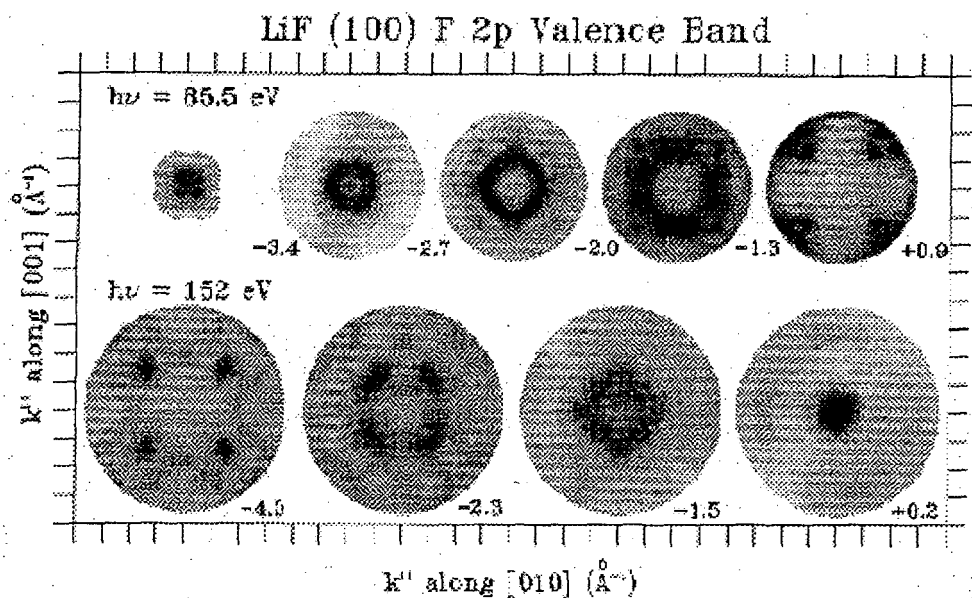
Figure 8: Angular distribution of photoelectrons from LiF, taken at various energies with a display spectrometer[15] Band dispersions obtained from these data indicate an expansion of the band width due to self-energy in this localized system.

reciprocal lattice vector $g^{\parallel}$ simply corresponds to plotting energy bands in a reduced surface Brillouin zone, i.e., within the unit cell in $k^{\parallel}$ space.

In the three-dimensional case, the momentum perpendicular to the surface, $k^{\perp}$, is conserved in the optical transition since a UV photon carries negligible momentum corrpared to crystal electrons. However, $k^{\perp}$ is not conserved during the escape of the photoelectron because of momentum transfer at the surface potential step. Several methods have been conceived to overcome this difficulty. They are reviewed in detail elsewhere.[3] In most of them the extra parameter deterrmining $k^{\perp}$ is the photor energy. Essentially, one moves along the $E_{\mathbf{u}}(k^{\perp})$ dispersion of an upper band by tuning the photon energy. The task is to get accurate information about this upper band in order to obtain $k^{\perp}$ from the energy $E_{\mathbf{u}}$ of the photoelectron (or the incoming electron in inverse photoernission). At first it looks like nothing has been gained by transferring the $k^{\perp}$ determination from a lower to an upper band. However, the upper bands become more and more free-electron-like as one goes higher in energy since the kinetic energy becomes large compared to the crystal potential.

Characteristic examples of current band mapping results are given in Figs. 6-8 (Refs. [13-15]). They are compared to the state of the art in band theory, represented by quasiparticle calculations. These calculations determine the energies of the quasiparticles that are actually measured, i.e. holes for occupied states and extra electrons for unoccupied states. Conventional calculations, such as the local density and Hartree-Fock methods determine only energy eigenvalues for the neutral ground state, which cannot be measured, even in principle. The effect of the so-called self-energy corrections that arise when going from a ground state to a quasiparticle calculation depends on the class of materials. For semiconductors (Fig. 6, Ref.[13]) the biggest effect is a correction to the band gap. It comes out too low by about a factor of two in local density and too high in Hartree-Fock. Germanium actually would be a metal in local density theory. Simple metals, such as Na in Fig. 7 (Ref.[14]), exhibit delocalized electronic states with a free-electson-like band structure. In this case the local density calculation gives the corsect Fermi surfaee, but the width of the occupied part of the band comes out too large by about 18%. In a somewhat oversimplified view the self-energy correction might be explained as extra screening of the holes, which pushes their energy towards the Fermi level. Insulators, such as LiF shown in Fig. 8 (Ref.[15]), represent the other end of the spectrum with very localized valence states. It appears that the reverse effect takes place here, i.e. a band widening due to the self-energy.

111.2 Spin and Helicity

Spin detection of photoelectrons and/or the use of circularly-polarized light open up the field of magnetic materials. The magnetic properties of thin films are particularly interesting since they may deviate strongly from the bulk properties. There are phenomena, such

as oscillatory magnetic coupling and giant magnetore- sistance, which can have direct impact on magnetic recording. We will give an example of such a structure in Section 111.5.

Near the surface of a magnetic film, or for a. magnetic monolayer one might naively expect a reduced magnetic interaction. After all, magnetism is a cooperative phenomenon, which should decrease when the number of magnetic neighbor atoms decreases. Indeed, for most thin films the Curie temperature is reduced, typically to half the bulk value at about 5 layers thickness. However, this is not the whole story. Diluting magnetic atoms actually should increase the magnetic moment for materials with a nearly half-filled d shell, e.g., V, Mn, Cr, Fe. In this case, the magnetic moment of an isolated atom is large, because Hund's rule aligns the spins. In a solid this spin alignment is partially quenched. Basically, Pauli's principle requires different spatial wavefunctions if the spin wavefunctions are equal, and in the solid there is not enough room for that. Although there are many theoretical predictions of this effect[16], there is only scarce experimental evidente, due to the difficulty in growing a flat monolayer of a magnetic material (with high surface energy) on an inert substrate (with low surface energy). In most cases one observes island formation or intermixing at steps and defects. If one were to chose a substrate with high surface energy the bonding across the interface would interfere with magnetism. There is an escape from this dilemma, however. By having a layer of a surfactant with low surface energy floating on top of the growing magnetic layer one can hope to keep the surface tension low and the layer flat. Due to this effect is has been possible to obtain some evidence[17] for enhanced magnetism for a monolayer of Fe on Au(100). The ferromagnetic exchange splitting of the 3d valence states obtained from spin-polarized photoemission and inverse photoemission is up to 40% larger than in the bulk. This points towards an enhanced magnetic moment, as we will see in the following.

The exchange splitting between minority spin and majority spin bands is a characteristic of the band structure of ferromagnetic materials. It can be measured by spin-polarized photoemission (Fig. 9, Refs.[18,19]). It is now possible to perform the "complete" photoemission experiment, where not only energy and momentum are determined, but also the spin and the point group symmetry via polarization selection rules.

Recently, it has been found empirically that the exchange splitting is correlated with the local magnetic moment (Fig. 10, Ref.[20]). This holds not only for ferromagnets, but also for antiferromagnets, and even

spin glasses and the free atoms, where there is no long range order. Local density calculations show this trend even clearer, i.e. an exchange splitting of about 1 eV per Bohr magneton.
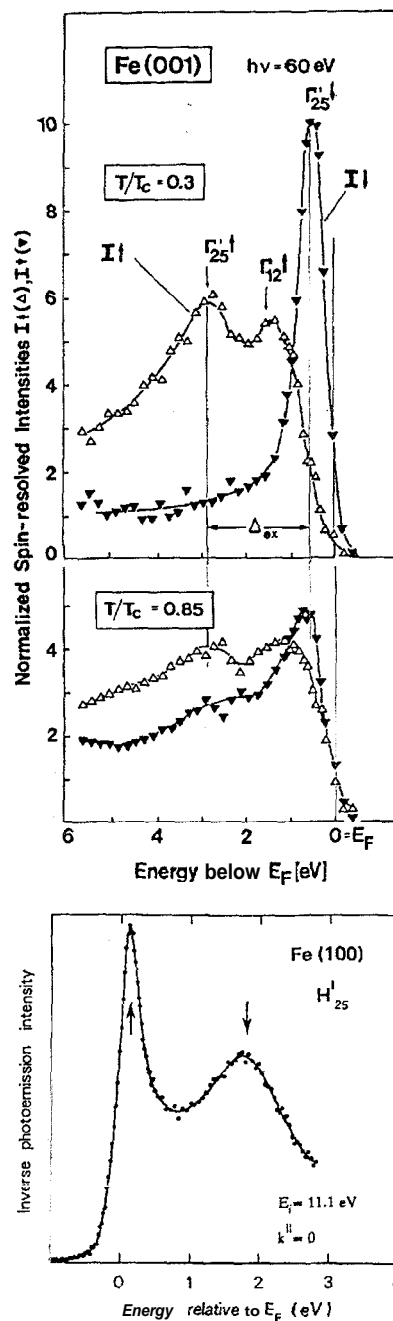

Figure 9: (a) Angle-, spin-, and symmetry-resolved photo-electron spectra[18] from Fe(100) at two ternperatures, showing the ferromagnetic exchange splitting between majority and minority spin bands and its development with temperature approaching the Curie temperature T_c. (b) Inverse photoemission spectrum[19] showing the analogous splitting for states above the Fermi level.
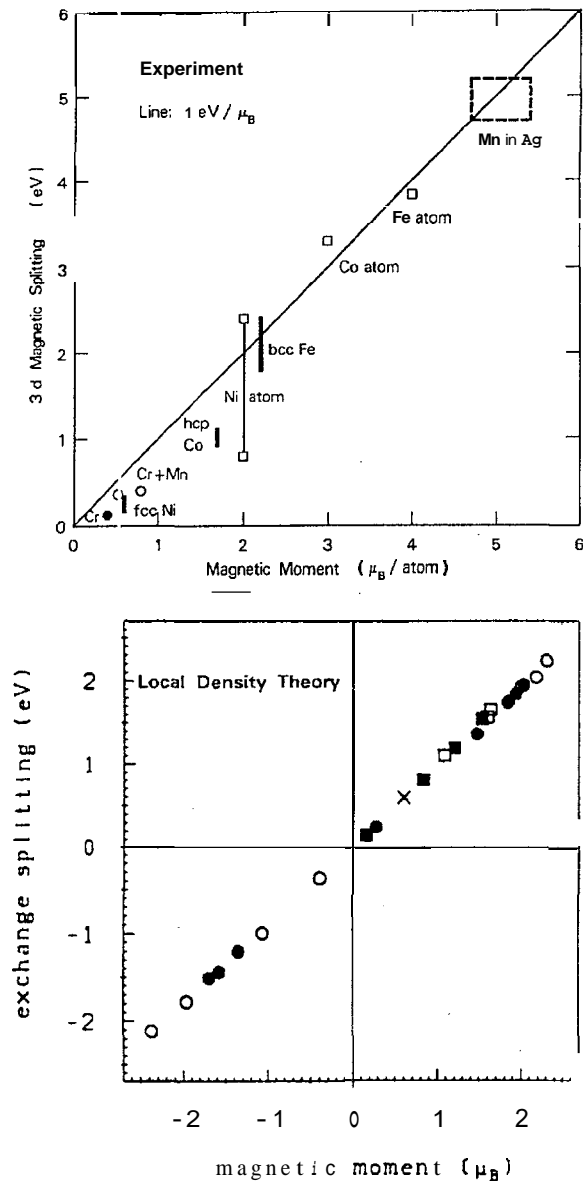
Figure 10: Correlation between the exchange splitting of the 3d states and the local magnetic moment[20]. Experimental data as well as local density calculations for various alloys give a relation of about $1eV/\mu_B$.

111.3 Fermiology

Electronic states at the Fermi level are of particular importance. All transport phenomena are governed by thermally-excited electrons or holes within typically kT of the Fermi level. Electronically-driven phase transitions are caused by a rearrangement of states within about kT_c of the Fermi level, where T_c is the transition temperature. Examples are superconductors, ferro- and antiferromagnets, and charge density waves. Such systems will be discussed in more detail in the article by Y. Petroff[4].

Low-dimensional systems exhibit a variety of peculiar phenomena that show up in the electronic struc-

ture near the Fermi level. Correlation effects increase in lower dimension, particularly in one-dimensional systems, where electrons cannot "pass" each other without occupying the "same" point in space. The correlations suppress the density of states at the Fermi level. Also, long-range order is suppressed in lower dimensions, leading to magnetically-dead two-dimensional layers (at least for Heisenberg and x,y systems) and to the Peierls distortion in one dimension. Here, we give some examples of two-dimensional systems.
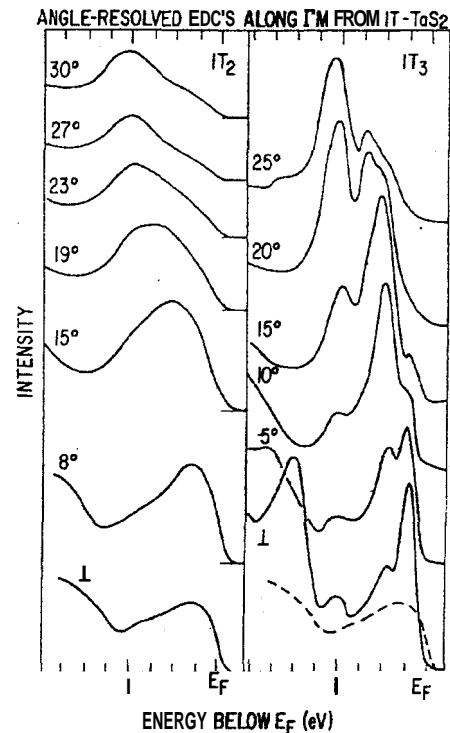

Figure 11: Metal-to-semiconductor transition[21] induced by a charge density wave in TaS_26. The Fermi edge moves down by 1/8 eV in the semiconducting $1T_3$ phase compared to the metallic $1T_2$ phase (dashed). Additional gaps open up below the Fermi level.

In Fig. 11 (Ref.[21]) the change of the electronic structure of TaS_2 across the phase transition from an incommensurate to a commensurate charge density wave is observed. The low temperature, commensurate phase has a small pseudo-gap at the Fermi level, which lowers the energy of occupied states just below the Fermi level and thus drives the phase transition energetically. (The density of states does not go to zero completely in the gap, as explained by Dardel et al.[21]. Therefore one talks about a pseudo-gap). The same effect is seen on a smaller energy stale for superconductors (Fig. 12, Ref.[22]; see Ref.[4] for details). In TaS_2, however, there is no pairing, and the pseudo-gap causes an increase in resistivity. It is interesting to notice that in this case the change in the electronic structure is not confined to the Fermi level. It appears that
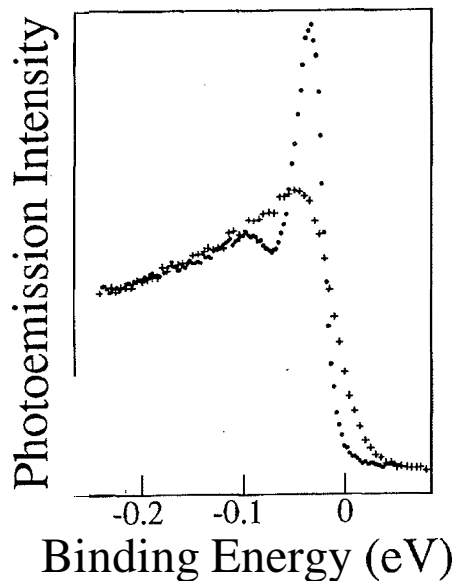
Figure 12: Opening of the superconducting gap around the Fermi level[22] in tlie high temperature superconductor $Bi_2Ca_2SrCu_2O_8$. The size of the observed gap and additional structure below E_F, indicate deviations from standard, weak coupling BCS theory.

there are gaps opening up throughout the Ta d-band, which are related to the new Brillouin zone boundaries in $\sqrt{13}$ x $\sqrt{13}$ reconstruction of the commensurate $1T_3$ phase (see tlie dips developing at 0.3 and 0.9 eV below the Fermi level in Fig. 11).

Surface states form a two-dimensional band structure, too. The corresponding two-dimensional Fermi surface tells us about driving forces for surface phonon softening and reconstruction, adsorbate bonding, and surface transport. Fig. 13 (Ref.[23]) shows an example.

A convenient way to map out Fermi surfaces in two-dimensional systems is shown in Fig. 14 (Ref.[24]). Instead of taking a series of spectra for tlie Fermi level crossing at each $k^{\parallel}$ point one may use a display-type spectrometer and image the whole Fermi surface in one shot. The example chosen here is peculiar, since graphite is a semimetal, where the Fermi "surface" degenerates into zero-dimensional spots at the corners of the hexagonal Brillouin zone, while normal two-dimensional systems exhibit one-dimensional Fermi lines. There are some current drawbacks of this imaging technique, but they are not fundamental. The distortion in Fig. 14 is due to the electron optics of the spectrometer, and can be removed numerically (see Fig. 8). The resolution of this particular type of display spectrometer is limited to about 0.05eV by work function inhomogeneities of the ellipsoidal mirror and the

retarding grid. Other designs do not have such a limit. But even giving up energy resolution completely and imaging all occupied states one still will get a sharp cutoff when going from occupied to unoccupied states at the Fermi wavevector. This cutoff is given by tlie Fermi function, which is much narrower than the analyzer resolution.

111.4 Surfaces and **Adsorbates**

Surface and adsorbate states have been the subject of very active research in the last decade. A number of reviews[3] have covered this topic. Here we restrict ourselves to demonstrate the basic phenomena with a few examples. Generally, two-dimensional states can form at surfaces as long as no three-dimensional bulk states of the same symmetry are available at the same energy E and parallel momentum $k^{\parallel}$. Even if there are some, the two-dimensional states often survive as resonances if the coupling to the bulk states is weak. The surface states discussed in the following are essentially localized in tlie first atomic layer. They may be viewed as broken bonds, e.g. the directional sp^3 bonds in semiconductors or the d orbitals of metals. There are, however, more delocalized surface states derived from s,p-states, whicli can extend as far as 10 layers into the bulk.

Surface states show up particularly well in the band gap of serniconductors. Figure 15 (Ref.[25]) shows that both occupied and unoccupied surface states exist in the gap at a group IV semiconductor surface. They reflect the fact that broken bonds are half-filled orbitals, which can be ionized in photoemission and filled witli inverse photoemission. By replacing surface atoms with group III or group V elements one is able to pull these surface states out of the gap, either emptying or filling the broken bond orbitals. Such surfaces are many orders of magnitude less reactive than the clean Si surface.

Figure 16 (Ref.[26]) serves to illustrate the bonding of adsorbates to metals. The situation is exceptionally-simple here since one essentially deals only with one Ti 3d orbital of d_{z^2} symmetry bonding to the 1s orbital of the H atom. The corresponding bonding and antibonding combinations can both be seen in the photoemission spectra at $k^{\parallel} = 0$. Even the lateral bonding within the H overlayer can be inferred from the dispersion of tlie bonding state, which has mainly H1s character. The H-H interaction is attractive at the Brillouin zone center $\bar{\Gamma}$, and repulsive at the zone boundary.
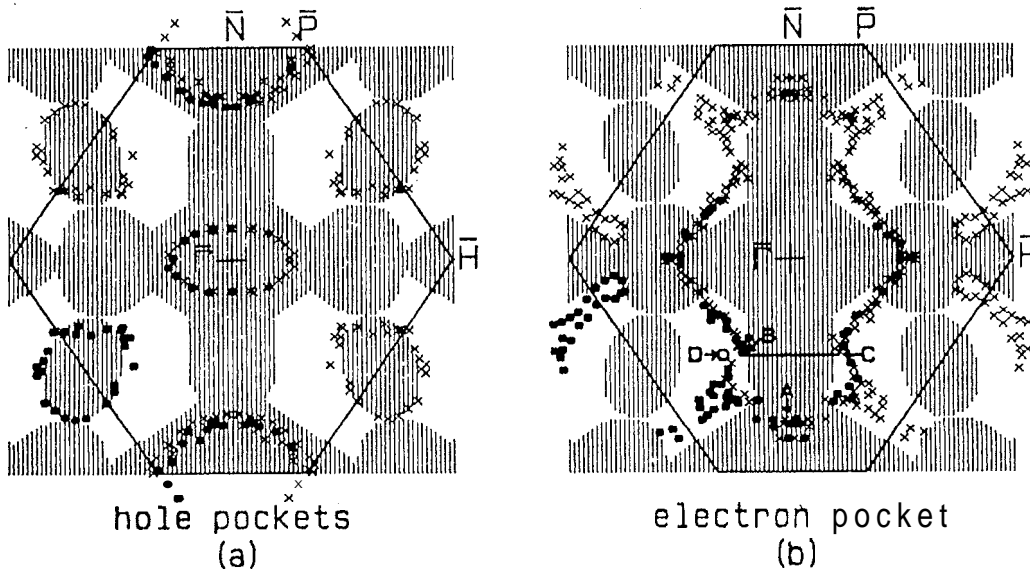
hole pockets   electron pocket
(a)   (b)

Figure 13: Fermi surfaces of surface state bands[23] on Mo(110) (symbols), shown on top of the projected bulk Fermi surface (hatched).

Figure 15: Broken bond states on Si(111) surfaces (hatched), mapped at $k^{\parallel} = 0$ by photoemission and inverse photoemission[25]. The clean surface has both occupied and unoccupied states in the gap, due to partially-filled broken bonds. By adsorbing group V or group III atoms the states become completely filled or completely empty. The peaks labelled L_3', Li, L_3 are bulk transitions common to all surfaces.
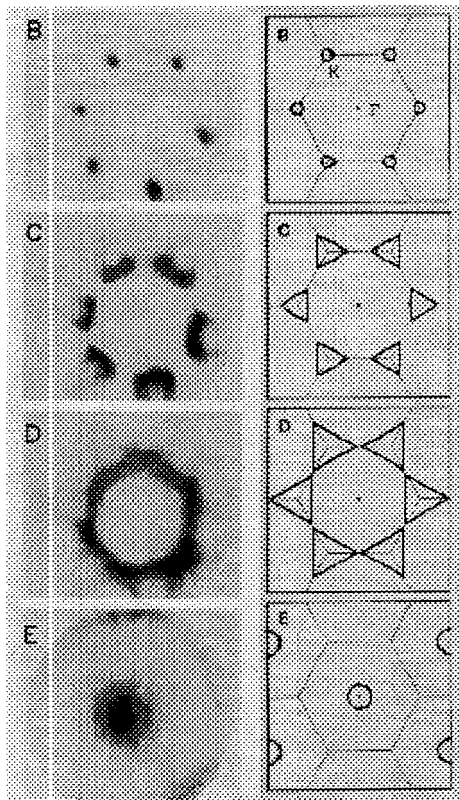
Figure 14: Direct imaging of equal energy surfaces in graphite[24]. The Fermi "surface" (B) degenerates into points, making graphite a semimetal.
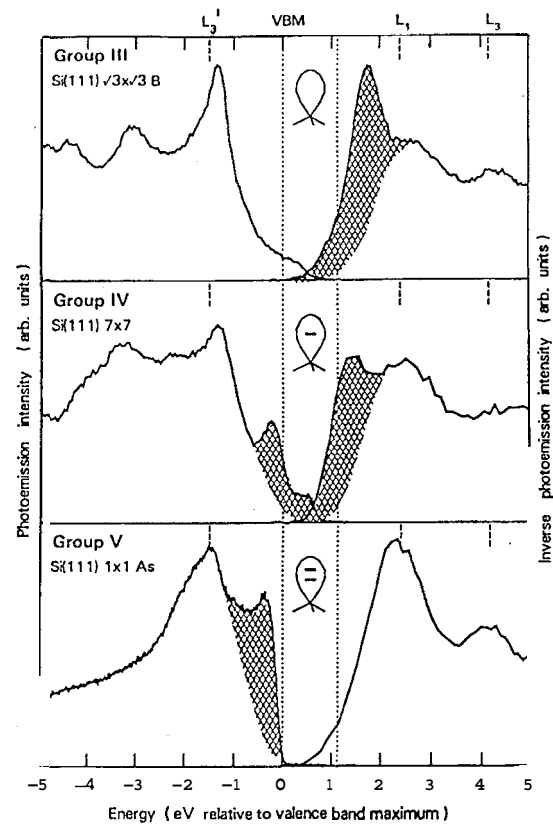
ADSORBATE BAND DISPERSIONS (CHEMISORPTION)
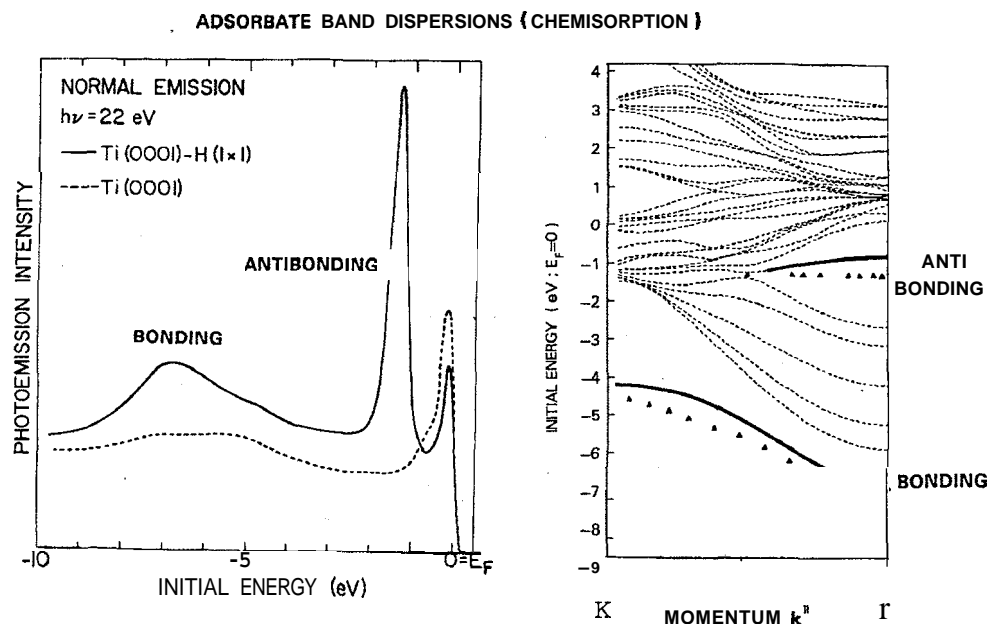

Figure 16: Bonding of H to a Ti(001) surface[26], demonstrated by photoemission and local density calculations. The T3dz_2 surface orbital at the Fermi level (dashed curve) forms bonding/antibonding combinations with the H1s orbital.

Orbitals of adsorbed molecules may be classified into two groups, i.e. the outermost, highest energy orbitals that are involved in chemical bonds to the substrate, and the deeper orbitals that reflect the intramolecular bonds. The latter can be used as a fingerprint of the adsorbed molecule, and tell us if it decomposed at the surface. An example is given in Fig. 17 (Ref.[27]), where the C2s states are used to identify various alkanes. In the ethyl groups of diethylsilane adsorbed on Si one sees the bonding/antibonding doublet of the C2s electrons from the two C atoms. For alkanes in general, one sees as many C2s levels as there are carbon atoms[28]. Such ligands occur in organometallic compounds that are used in the chemical vapor deposition of semiconductors. The particular compound shown here has been studied as a candidate for atomic layer epitaxy of Si (compare Section IV.2).

The antibonding σ^* and π^* orbitals of adsorbed molecules are good examples for outer orbitals. They are mostly unoccupied, and can be probed with inverse photoemission or core level absorption spectroscopy. In Fig. 18 (Ref.[29]) an example is given for the latter technique, using Auger electrons as a measure of the number of core holes created in the absorption process. The polarized nature of synchrotron radiation is utilized to determine the orientation of the orbitals, and thus the orientation of the molecule. This simple technique works also for solids. For example the orientation of the superconducting states in high temperature su-

perconductors has been determined in the same way[30].

III.5 "Engineered" Solids

Surface science has made enormous progress in the past decade. We are now at a point where just about any question about the electronic and atomic structure of surfaces can be solved with the available techniques. At this point one can start using the tools of surface science to arrange atoms at surfaces in such a way as to obtain new materials with particular properties. Perpendicular to the surface one may build up multilayers with atomic precision, i.e. layer by layer. Parallel to the surface one could move atoms around with a scanning tunneling microscope to produce low-dimensional structures. One-dimensional quantum wires might be grown along steps. Manipulation of clusters offers similar opportunities. The general idea is the same as in organic chemistry, i.e. synthesizing a new, often metastable structure, which exhibits specific, preplanned properties. In terms of the electronic properties one can achieve the largest effects by growing dissimilar materials on top of each other. For example, growing an insulator on a semiconductor one can change the interface band gap by a factor of two to five[31] (in the case of CaF_2 on Si(111)). Likewise, one can convert a semimetal into a semiconductor at the interface[32] (Sb or Bi on GaAs(110)), or change the magnetic properties[33] (see below). All these effects happen at the interface, where new bonding configurations are frozen in by the geometrical constraints.

Figure 18: Using polarization selection rules to determine the orientation of adsorbed molecules[29]. The σ orbitals are excited from a 1s level by the electric field vector along the molecular axis, the a orbitals by the perpendicular component.
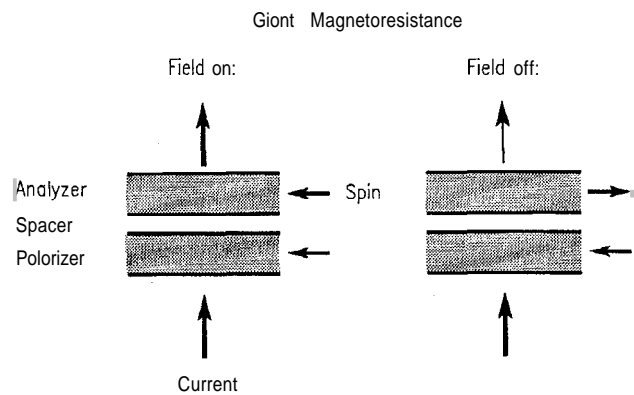
Figure 19: Explanation of a bulk effect contributing to the giant magnetoresistance in magnetic multilayers. Since majority spin electrons have a much longer mean Gee path at the Fermi level than minority spin electrons, they become majority spin-polarized in the first magnetic film (polarizer), and are attenuated by a second film with opposite spin direction (analyzer). By flipping the spin of the second film with an external field the transmitted current increases. In addition, there is an interface effect due to different reflectivities for the two spin directions.
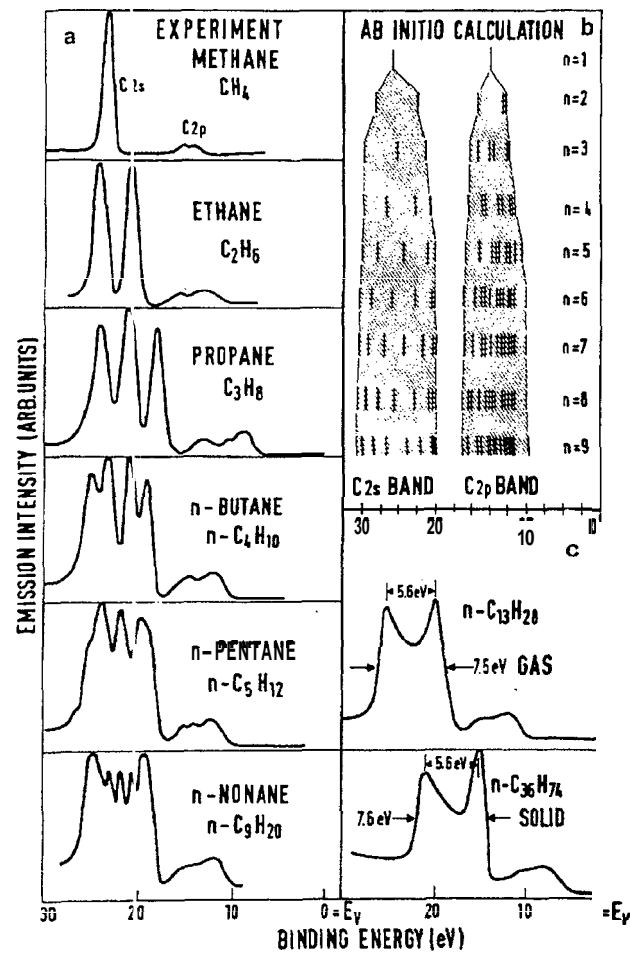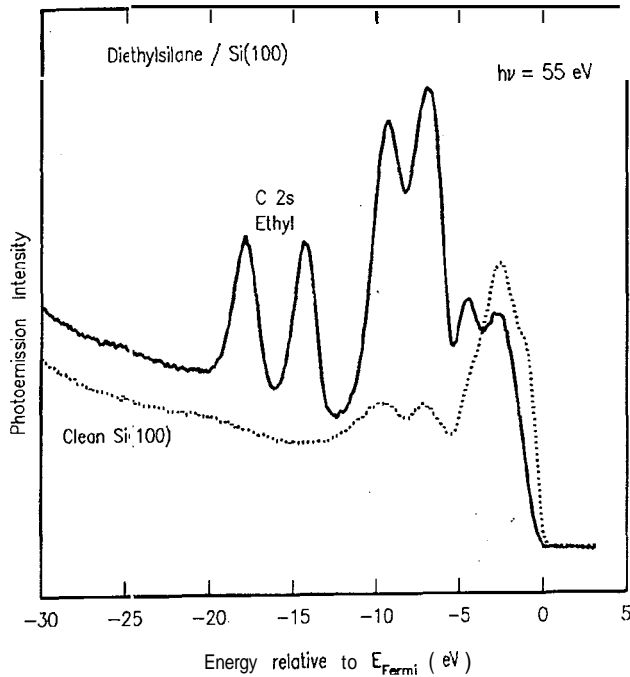

Figure 17: E'ingerprinting of adsorbed molecular species by their deeper molecular orbitals[27,28] which are not involved in the bond to the surface. Here the splitting of the C2s orbital indicates ethyl groups on Si(100). Different alkanes can be identified by the number of C2s peaks.
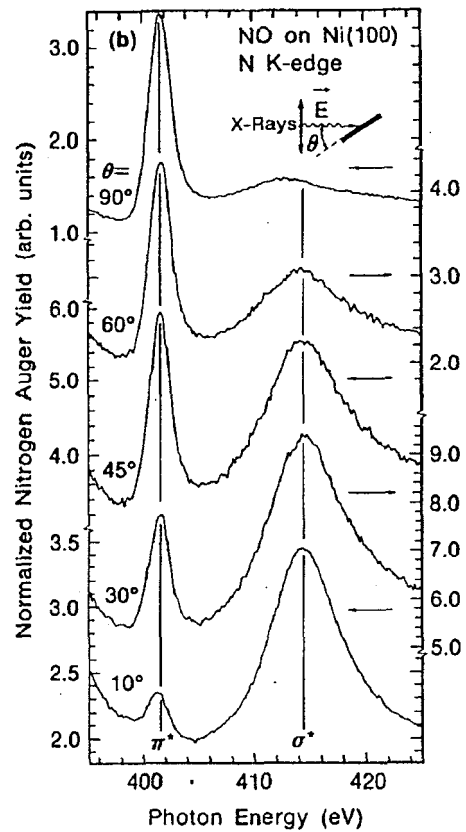
Therefore it is also important to grow multilayer structures with periodicities in the order of an atomic layer, such that most of the artificial solid consists of interface atoms.

As an example we will discuss magnetic superlattices, which have generated a lot of interest recently by their unusual properties, such as oscillatory magnetic coupling and "giant" magnetoresistance[33]. The latter has possible applications in magnetic recording. The state of the art in magnetic reading heads uses the magnetoresistance in permalloy, which is only a 2% effect. Multilayer structures offer an order of magnitude larger changes in resistance, thus enhancing the sensitivity to the signal from a magnetically-stored bit pattern. For magnetic multilayers we are just about able to predict what type of coupling (ferromagnetic or antiferromagnetic) a structure of alternating ferromagnet and noble metal layers will have, and how many noble metal spacer layers it will take to achieve a certain coupling.

Before getting into the band structure of magnetic multilayers it is useful to understand the intended electronic properties, such as giant magnetoresistance. Figure 19 gives a highly-simplified explanation of such a change in resistance caused by a magnetic field. The spin valve structure shown in Fig. 19 contains two magnetic layers separated by a nonmagnetic spacer. The giant magnetoresistance effect occurs only if the two magnetic layers prefer the unusual configuration with opposite magnetization directions. Then an external field is able to change the magnetic configuration by forcing both magnetizations to be parallel. The idea is to specifically design such materials, either by choosing the proper spacer layer thickness or by adding a fourth, magnetic layer to bias the structure magnetically. Understanding the magnetic coupling is essential for this purpose. The observed lowering of the electrical resistivity with the external field can be rationalized by a simple model where one magnetic layer acts as a polarizer by generating a polarized current of majority spin electrons at the Fermi level, the other as analyzer by transmitting preferably majority spin electrons. The fact that majority spin electrons are the preferred charge carriers in magnetic materials can be explained by their longer mean free path compared to minority spin electrons at the Fermi level. The majority spin d-band is filled in many ferromagnets (e.g. Co and Ni), making the band structure similar to that of a noble metal, where only a low density of s,p states is available at the Fermi level to scatter electrons by electron-hole pair production. The minority spin band structure, on the other band, has a much highest- density of d-states at the Fermi level, producing more electron-hole pairs with minority spin electrons. (Note that spin-flip scattering is much less probable, such that it

can be neglected in this simple argument). Although structures with the current perpendicular to the layers, as in Fig. 19, exhibit very large magnetoresistance[34] the structures used in practice have the current parallel to the layer, in order to obtain reasonable resistivities. That generates extra complications, though, since the non-magnetic spacer tends to short out the magnetic layers. A certain interface roughness is needed to get enough bounces off the magnetic layers, but too much roughness kills the electronic states that cause the antiferromagnetic coupling, as we will see below. In addition, the interfaces themselves exhibit strongly spin-dependent reflectivities, giving rise to additional magnetoresistance[33]). Thus there is ample room for innovative ideas of new structures that optimize the desired magnetoresistive effect.

In the search for the electronic states that cause oscillations in the magnetic coupling of multilayers one has to understand electronic states of thin films. As Fig. 20 (Refs.[35,36]) shows, the continuum bulk band dispersion becomes discretized along the direction perpendicular to the interface when electrons are confined to a thin film. The number of discrete states per band corresponds to the number of atomic layers in the film. This discretization can be seen for thin $Cu(100)$ films in Fig. 21 (Ref.[36]), which have a band structure very similar to the $Ag(100)$ film in Fig. 20. For states relevant to magnetotransport and coupling we look at the density of states at the Fermi in Fig. 22 (Ref.[36]). Indeed, we observe discrete thin film states crossing the Fermi level with a periodicity similar to the magnetic period (about 6 atomic layers). Instead of viewing the intensity oscillations as discrete states moving across the Fermi level we also may consider these films as the world's smallest Fabry-Perot interferometers, with density of states maxima corresponding to interference fringes appearing every half wavelength. The appropriate wavefunction of electrons in a thin film is shown schematically in Fig. 23 (Ref.[36]). It contains a fast-oscillating Bloch function, derived from the nearest band edge, and a slowly-varying envelope function that ensures the proper boundary conditions at the interfaces. The latter gives rise to the intensity oscillations. These discrete thin film states can become spin-polarized by spin-dependent boundary conditions at the interface to the ferromagnet. Having understood the states in the spacer layer between the magnetic layers we can go ahead and design multilayer structures with the desired magnetic properties. It turns out that the periodicity of the magnetic coupling is given by a bulk property of the spacer layer (i.e. its Fermi surface), while the phase of the oscillations is a bulk property of the magnetic material (i.e. its spin-dependent band gaps).
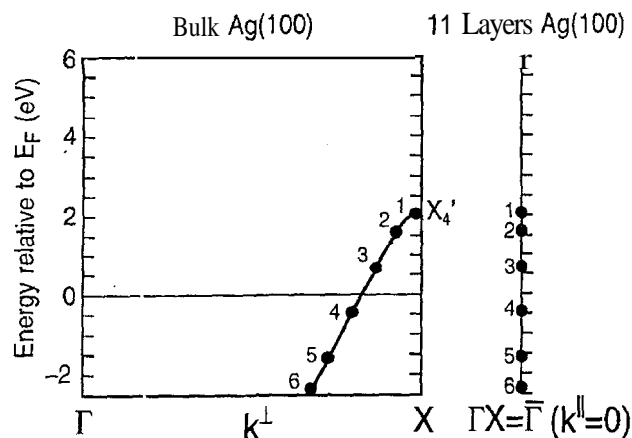
Bulk Ag(100)   11 Layers Ag(100)

Figure 20: Discretization of bulk bands in a thin film (from local density calculations[35]). The number of discrete states per band corresponds to the number of atomic layers in the film.

Figure 21: Obsrrvation of discrete thin film states (numbered) in Cu(100) films with inverse photoemission[36]. The layers were grown epitaxially on fcc Fe(100), which in turn was grown epitaxially on Cu(100).
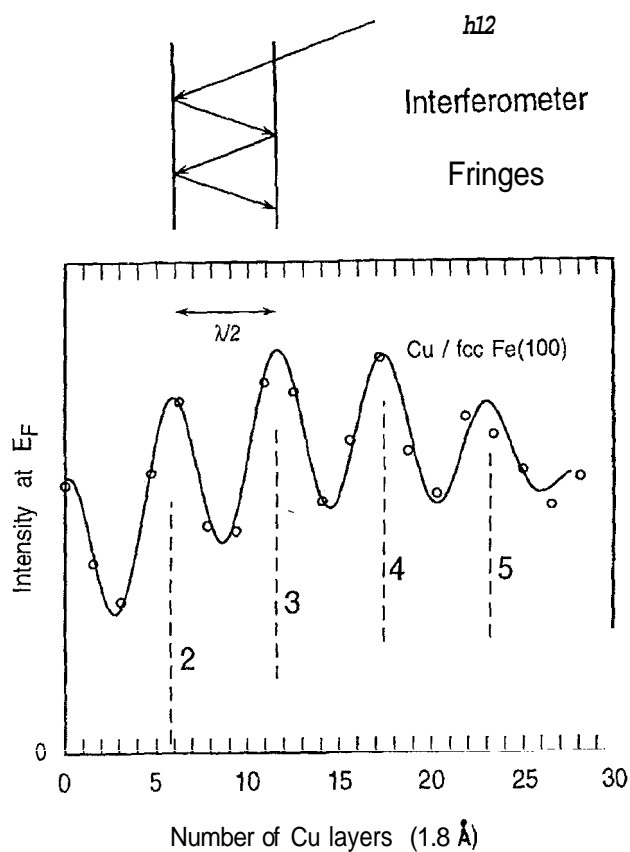

Figure 22: Intensity at the Fermi level versus film thickness from Fig. 21 (Ref.[36]). The maxima correspond to discrete thin film states crossing the Fermi level. They may also be viewed as interference fringes of the envelope wavefunction of the electrons (see Fig. 23).
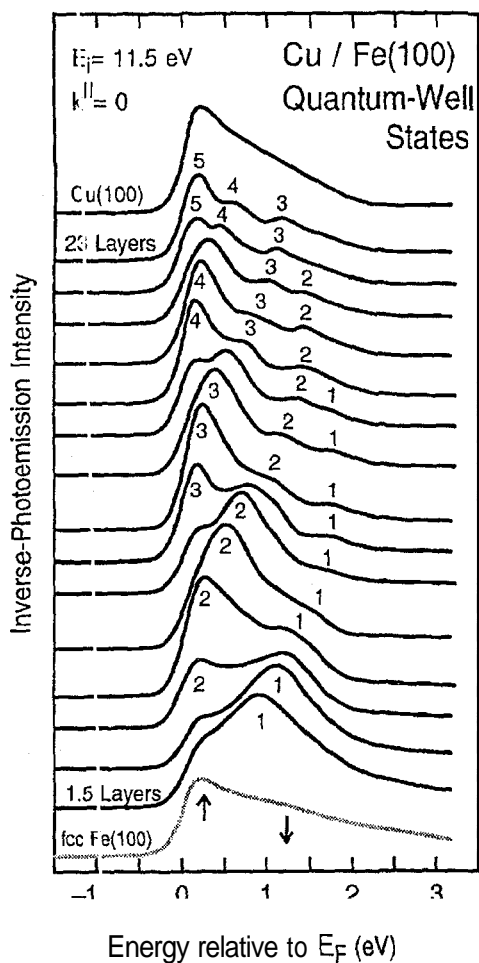
Another set of materials that has attracted recent interest are the fullerene carbon clusters. Cluster physics in general has been an area full of interesting surprises concerning rapid changes in the electronic structure and chemical reactivity with cluster size. What sets the C_{60}, C_{70}, and similar clusters apart is their chemical stability and the availability of macroscopic quantities of pure clusters. Here we just show the use of tunable synchrotron radiation in mapping the empty π^* and σ^* orbitals by absorption spectroscopy from the C1s core level (Fig. 24, Ref.[37]). It is surprising that clusters containing as much as 60 and 70 atoms still are electronically quite different from each other and by no means have reached the orbital structure of their infinite analog, i.e. graphite. As with multilayers, the carbon clusters exhibit a lot of flexibility for chemical tuning by substitution, insertion and addition of extra atoms.
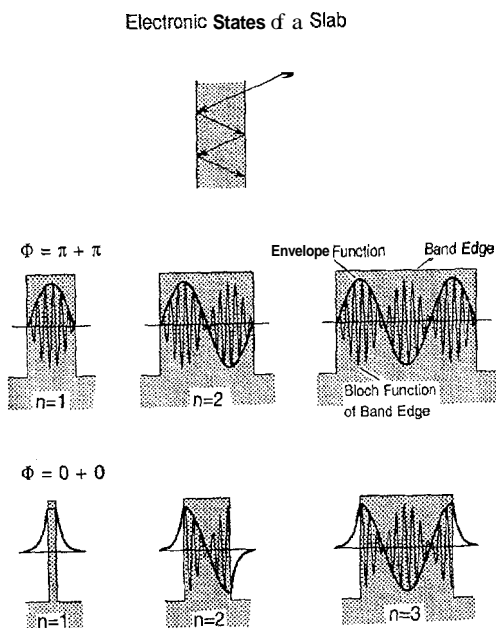
Electronic States of a Slab

$\Phi = \pi + \pi$

Envelope Function   Band Edge

n=1   n=2   Bloch Function of Band Edge

$\Phi = 0 + 0$

n=1   n=2   n=3

Figure 23: Wave function of discrete thin film states, or quantum well states[36]. The rapidly-oscillating Bloch function derived from the edge of a bulk band (hatched area) is modulated by an envelope function that ensures the proper boundary conditions.
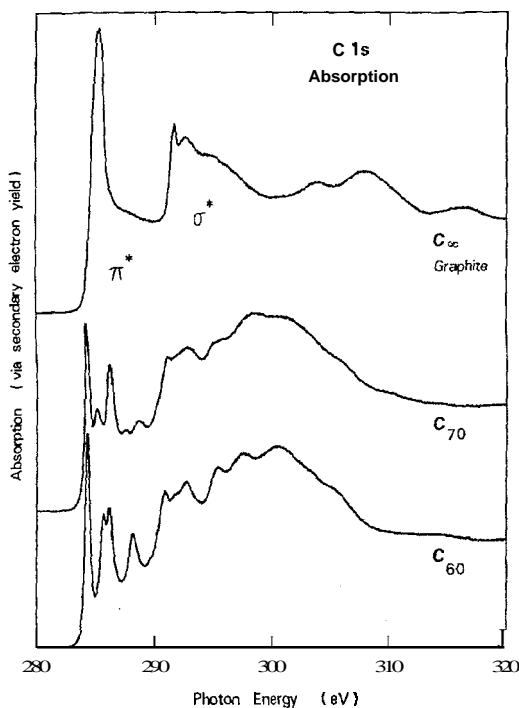

C 1s
Absorption

σ^*

π^*

C_∞
Graphite

C_{70}

C_{60}

Absorption (via secondary electron yield)

280   290   300   310   320

Photon Energy (eV)

Figure 24: C1s absorption spectra of fullerenes compared to their infinite analog graphite[37]. Significant changes between C_{60}, C_{70}, and graphite are seen for the transitions into π^* orbitals, showing that the electronic structure depends sensitively on cluster size, even for large clusters.

IV. Core Levels

Tlie structure and composition of many surfaces (interfaces) encountered in technoiogy is much too complex for performing complete angle-resolved photoemission studies and for calculating the band structure from first principles. When long-range order is lost one has to resort to simpler probing techniques and must concentrate on determining the short-range order and the local properties, e.g. coordination, valence, oxidation state. Core levels are well-suited for this purpose. They are not affected by the loss of long-range order because of their localized nature. The core level binding energy has a simple relation with chemical properties, e.g., charge transfer and oxidation state.

The use of synchrotron radiation has given a great boost to the field. Monolayer surface sensitivity can be achieved by tuning the photon energy to 30-50eV above threshold, where the pliotoelectrons come out with the minimum escape depth. Under these conditions the escape depth can be as short as 3Å (two layers) compared to about 20Å (more than 10 layers) in conventional X-ray photoelectron spectroscopy (XPS). This short escape depth makes it possible to detect a monolayer of chemically altered atoms at a surface or an interface.

The photon energy range to be covered is determined by the binding energies of the sharpest core levels of each element. As shown in Fig. 25, it ranges up to 1 keV. While it is possible with current synchrotron sources to cover binding energies up to about 200eV with a photon and electron energy resolution comparable to the intrinsic width, it will require undulator sources, such as the Advanced Light Source (ALS) to access the deeper core levels with the intrinsic resolution limit and good count rates. These elements include the "organic" group (C, O, N, F) and the 4d and 5d transition and noble metals. Exploratory experiments have shown that it will be possible to distinguish inequivalent C atoms in organic compounds and polymers, and follow their chernical reactions. In the following we will demonstrate the capabilities of core level spectroscopy for the Si2p level, which is one of the most extensively studied core levels (see Ref.[38]).

IV.1 Core Level Shifts: Mostly Si2p

Core level shifts can have a variety of causes, such as band bending (see Fig. 26, Ref.[38]), charge transfer, and relaxation. We are mainly looking at the chemical and relaxation shift between of the outermost atomic

The Sharpest Core Levels and ther Binding Energies (eV)

H 1s 14																	He 1s 25
Li 1s 55	Be 1s 112											B 1s 189	C 1s 284	N 1s 410	O 1s 543	F 1s 543	Ne 1s 870 2p 22
Na 2p 31	Mg 2p 49											Al 2p 73	Si 2p 100	P 2p 135	S 2p 163	Cl 2p 200	Ar 2p 248 3p 16
K 2p 295 3p 18	Ca 2p 346 3p 25	Sc 2p 399	Ti 2p 454	V 2p 512	Cr 2p 574	Mn 2p 639	Fe 2p 707	Co 2p 778	Ni 2p 853	Cu 2p 933	Zn 3d 10	Ga 3d 19	Ge 3d 29	As 3d 42	Se 3d 55	Br 3d 69	Kr 3d 94 4p 14
Rb 3d 112 4p 15	Sr 3d 134 4p 20	Y 3d 156	Zr 3d 179	Nb 3d 202	Mo 3d 228	Tc 3d 253	Ru 3d 280	Rh 3d 307	Pd 3d 335	Ag 3d 368	Cd 4d 11	In 4d 16	Sn 4d 24	Sb 4d 32	Te 4d 40	I 4d 50	Xe 4d 68 5p 12
Cs 4d 78 5p 12	Ba 4d 90 5p 15	La 4d 103	Hf 4f 14	Ta 4f 22	W 4f 31	Re 4f 41	Os 4f 51	Ir 4f 61	Pt 4f 71	Au 4f 84	Hg 5d 8	Tl 5d 13	Pb 5d 18	Bi 5d 24	Po 5d 31	At 5d 40	Rn 5d 48 6p 11
Fr 5d 58 6p 15	Ra 5d 68 6p 19	Ac 5d 80															

Ce 4d 109 4f 1	Pr 4f 3	Nd 4f 5	Pm 4f 5	Sm 4f 5	Eu 4f 2	Gd 4f 8	Tb 4f 2	Dy 4t 4	Ho 4f 5	Er 4f 5	Tm 4f 5	Yb 4f 1	Lu 4f 7
Th 5d 85	Pa 5d 94	U 5f 1	Np 5f	Pu 5f 2	Am 5f	Cm 5f	Bk 5f	Cf 5f	Es 5f	Fm 5f	Md 5f	No 5f	Lw 5f

Figure 25: Binding energies of the sharpest core levels of all the elements. Photon energies up to 1 keV are required to ionize them.

layer. Band bending gives rise to an overall shift of the spectrum relative to the Fermi level, since the probing depth is usially much shorter than the depth of the band bending region. Bulk and surface effects can easily be separated by taking spectra with different photon energies. corresponding to different electron escape depths. Nesr threshold one has a probing depth of about ten layers, whereas at $h\nu = 130$eV one probes only two layers (see section IV).

Figure 2" (Refs.[38,39]) demonstrates surface core level shifts induced by adsorbates with opposite electronegativities. Oxygen pulls electrons of Si and increases the binding energy of the Si core electrons by creating a positive electrostatic potential. Ca does the opposite. After taking out the secondary electron background and clecomposing the spectrum into the $Si2p_{3/2}$ and $Si2p_{1/2}$ spin orbit components one can clearly distinguish four discrete surface core levels for oxidized Si. They are ass gned to Si bonding to one, two, three and four oxygen stoms, which may loosely be called $Si^{1}+$, $Si^{2}+$, $Si^{3}+$, and Si^{4+} ($Si^{4}+$ is the bonding configuration of SiO_2). The other three intermediate oxidation states are only stable at the interface, and disproportionate in bulk form. Exploiting a connection between core level shift and electronegativity difference, we compare the core level shift per ligand with the electronegativity difference between ligand and silicon in Fig. 28 (Ref.[38,40]). Ernpirically, there seems to be a correlation although exceptions exist, such as alkali metals. For small electronegativity difference $\Delta\chi$ the core level shift A E is nearly equal to $\Delta\chi$, at larger $\Delta\chi$ the core level shift sat rates, probably due to a saturatiori of the

charge transfer. From such an empirical curve one may predict core level shifts for new ligands, or find out from a measured core level shift which ligand is involved. An example is Ca-Si vs. F-Si bonding at the $CaF_2/Si(111)$ interface (see Section IV.4).

For C the core level shifts are about twice as large[41] as for Si, since the transferred charge sits in valence orbitals that are closer to the core than in Si. Such large shifts make core level spectroscopy of light elements even more attractive.

For a quantitative understanding of core level shifts, one has to take a variety of mechanisms into account[38,42]. These can be classified into initial-state and final-state effects. The former are due to a change in the chemical environment of a surface atom *and* comprise charge transfer, Madelung energy and rehybridization. The latter occur after the core level is ionized and can be viewed as a change in dielectric screening at the surface. One of the advantages of Si surfaces is that the dielectric constant of Si is so large (E M 12) that the screening is nearly complete, like in a metal (the image charge screening of surface charges is $((r - 1)/(\epsilon + 1))$. e ≈ 0.85 e for Si). Therefore, even with a reduced number of Si neighbors at the surface, there is still nearly complete screening. Consequently, the final-state effect is minimized, and long-range fields in the initial state, like the Madelung potential, are mostly screened out.

Looking at core level shifts at a higher level of sophistication one has to take vibrational sidebands into account. These phenomena represent a current frontier in gas phase spectroscopy. Examples for the the Si 2p
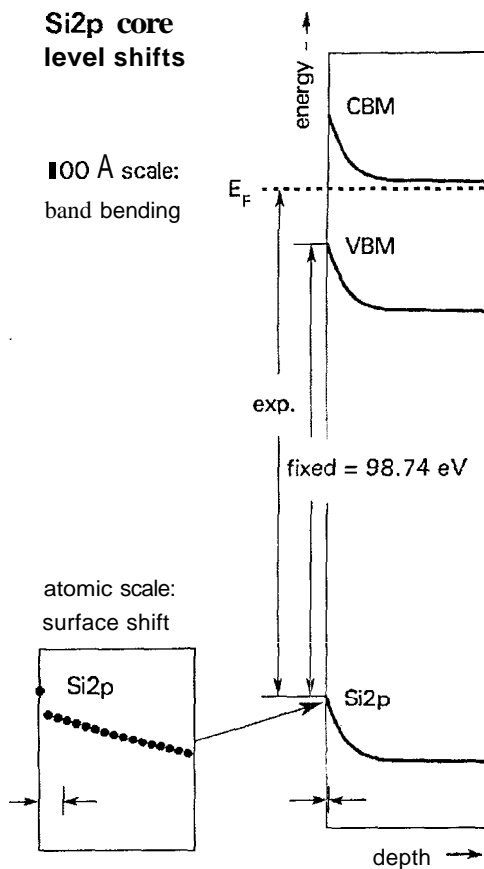
**Si2p core
level shifts**

100 Å scale:
band bending

atomic scale:
surface shift

Figure 26: Various types of core level shifts on a semiconductor surface[38]. A typical probing depth of synchrotron radiation experiments (indicated by double-arrows) allows to distinguish the shifted core level of the outermost atomic layer. Changes in band bending show up as an overall shift of the spectrum.
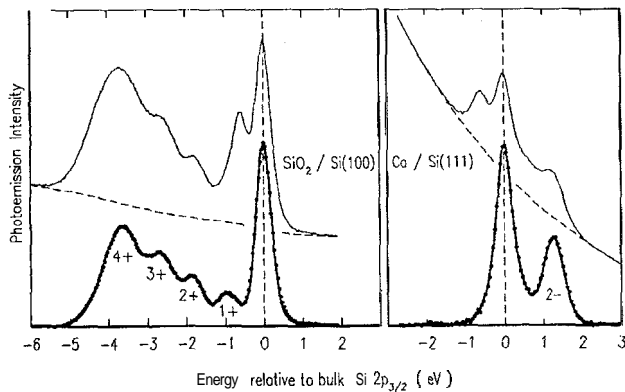

Figure 27: Opposite chemical shifts of the Si2p level induced by electropositive and electronegative adsorbates[38,39]. In order to see the shifts clearly the secondary electron background and the Si2p$_{1/2}$ spin-orbit partner have been removed for the bottom curves.
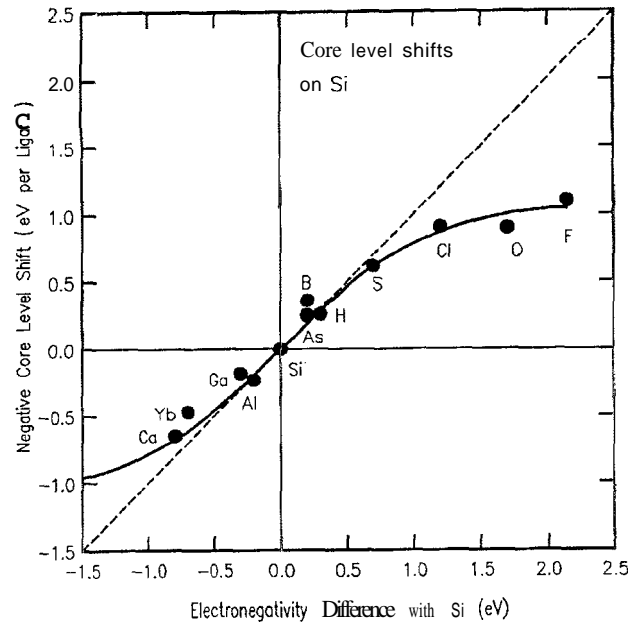

Figure 28: Correlation between the Si2p core level shift per ligand and the Pauling electronegativity difference[38,40]. The saturation of the curve is mainly due to a saturation of the charge transfer at large electronegativity difference. i.e. the core level shift is roughly proportional to the charge transfer.

levels of SiH_4 and SiF_4 are given in Fig. 29 (Ref.[43]). Depending on the size of the vibrational quanta the lineshape of the spectrum can be altered quite dramatically. Such spectra may be used to study the vibrational force constants and bond lengths of radicals using the equivalent core approximation. An atom of atomic number Z with a core hole is equivalent to a Z + 1 ion, i.e. Si with a core hole behaves like P^+.

IV.2 Semiconductor Surface Chemistry

The microelectronics technology has developed elaborate methods for processing surfaces and fabricating microstructures, particularly on semiconductors. The trend is away from classical, "wet" chemistry methods, and towards "dry" processing in a gas or plasma atmosphere. The most popular methods are reactive ion etching (RIE) for removing material, and CVD (chemical vapor deposition) for deposition. Over the years these methods have become extremely sophisticated. For example by small additions to the gas mixtures one can etch specifically Si, but not SiO_2, or the reverse. Likewise, it is possible to deposit W on Si for electric contacts without having it deposited on SiO_2 and shorting out the contacts. Most of these recipes have been obtained by trial and error, since there was not enough time for basic studies in the rapidly progressing field
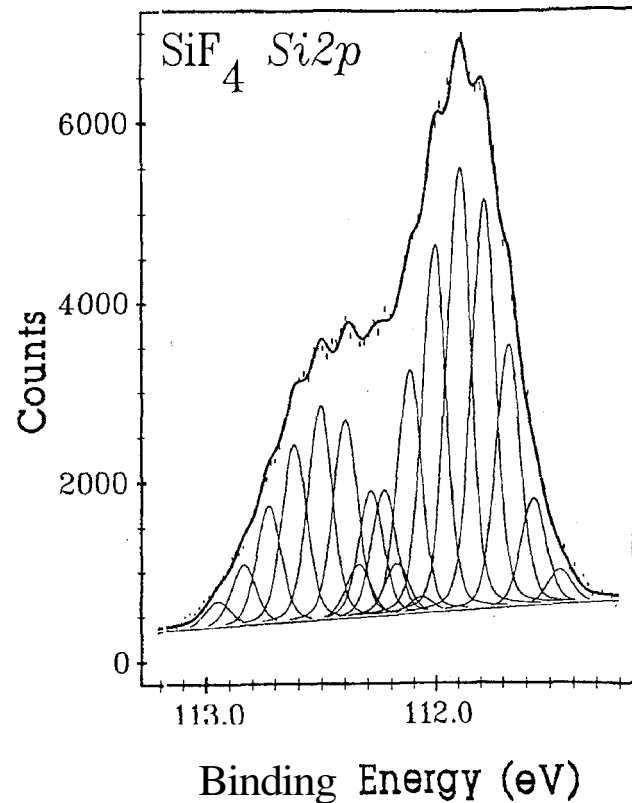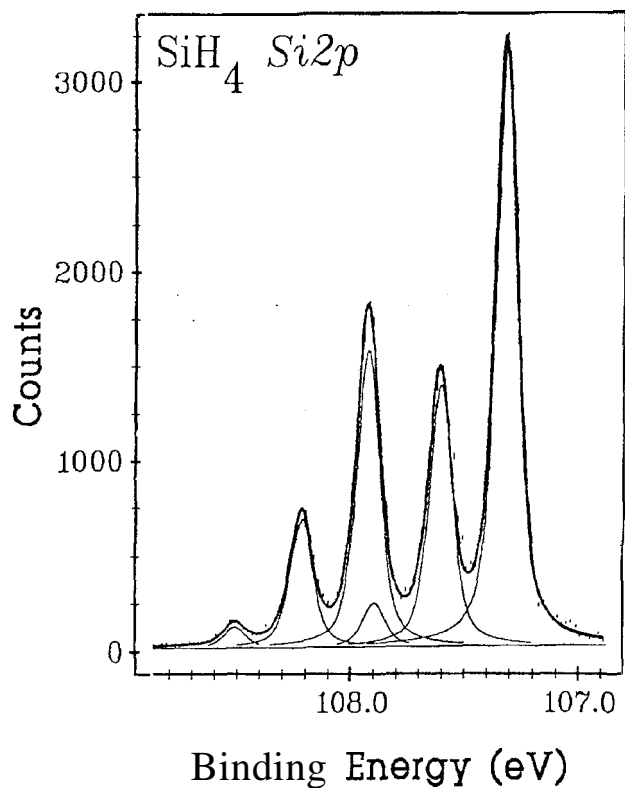
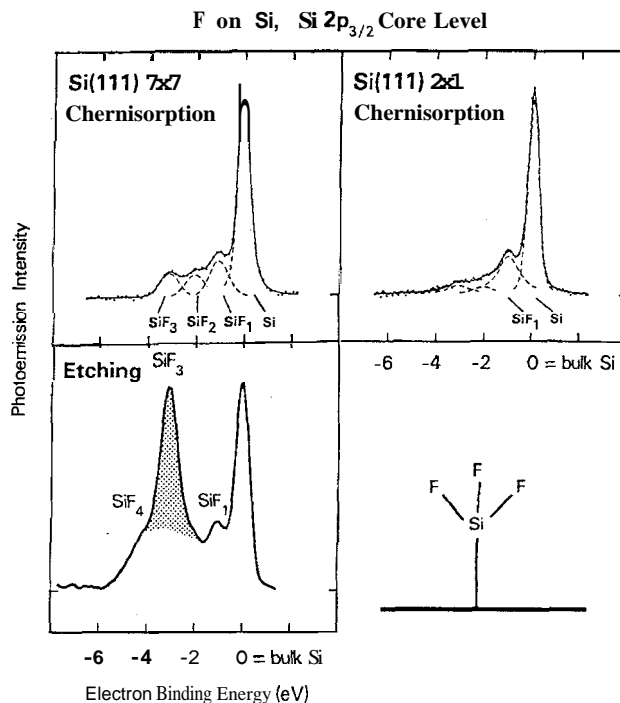Figure 29: Vibrational fine structure[43] of the Si2p spectrum in SiH₄ and SiF₄.

Figure 30: $Si2p_{3/2}$ spectra of F adsorption and etching on silicon[41]. The residue left on the surface after etching is SiF_3, showing that the bottleneck of the surface etching reaction is the removal of SiF_3 species.
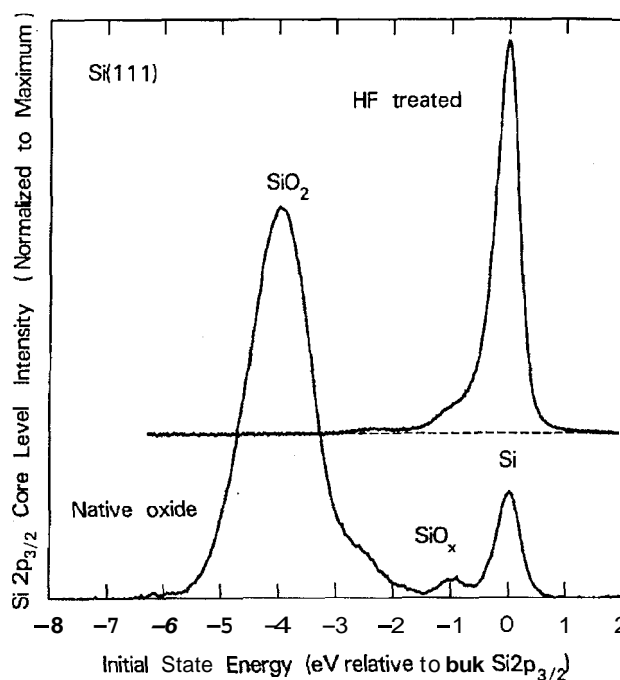

Figure 31: $Si2p_{3/2}$ spectra for a HF-passivated Si surface[44]. The surface is mainly H terminated and Gee of SiO_2, making it a good substrate for subsequent epitaxial growth via CVD (chemical vapor deposition).

semiconductor devices. Particularly poorly understood were the surface reactions, even though they represent the rate-limiting step in many cases. In recent years there has been a boom in exploring these surface reactions using surface-sensitive core level spectroscopy, particularly of the Si 2p level. By tuning into the escape depth minimum (about 130-150 eV photon energy for Si 2p) one can easily detect sub-monolayer amounts of adsorbed species, and determine their bonding using the simple correlations between electronegativity and core level shift. In the following we will always show the spin-orbit decomposed Si2p spectrum, which is much easier to read than a fit to the raw data.

Figure 30 (Ref.[41]) serves as an example from the etching arena. The top panels represent calibration experiments, where F as the likely active ingredient is adsorbed on well-defined Si surfaces in monolayer amounts. From there one can determine the core level shift versus the number of ligands. On the bottom the spectrum of a "real" surface is shown that has undergone steady-state etching. It exhibits a large peak associated with Si bonding to 3 fluorine atoms. The removal of these SiF_3 species thus must be a rate-limiting step of the surface reaction. This rather straightforward result was quite a surprise at the time, since the common opinion was that SiF_2 was the left-over species. It is actually the least-abundant according to the core level measurement.

The example in Fig. 31 (Ref.[44]) bridges between etching and deposition. It shows a Si surface with its native oxide, and after etching the oxide off with a very pure 10% HF solution. Such a treatment has been used to obtain clean starting surfaces for the deposition of high-quality, epitaxial Si with low temperature CVD. Devices made with this process hold several current speed records. As the Si 2p core level spectrum shows, there is no SiO_2 detectable on the surface within the detection limit of about one hundredth of a monolayer. Most of the surface is terminated with H, which induces a core level shift too small to be clearly resolved from the bulk line. Only about one tenth of the surface Si is bonded to F, OH, and sub-oxides. All these species can be removed by silane in the growth process, whereas SiO_2 cannot. It is somewhat surprising that the surface is terminated by H, and not by F, which bonds more strongly with Si. The detailed surface reactions in HF etching are the subject of current studies[45].

In the arena of growth we focus onto an example of a technique called atomic layer epitaxy (ALE), which has a promising future but has not been harnessed yet.

The idea is to deposit various materials exactly layer by layer in a two step procedure, adsorbing a self-limited monolayer first, and activating it by radiation, heat or
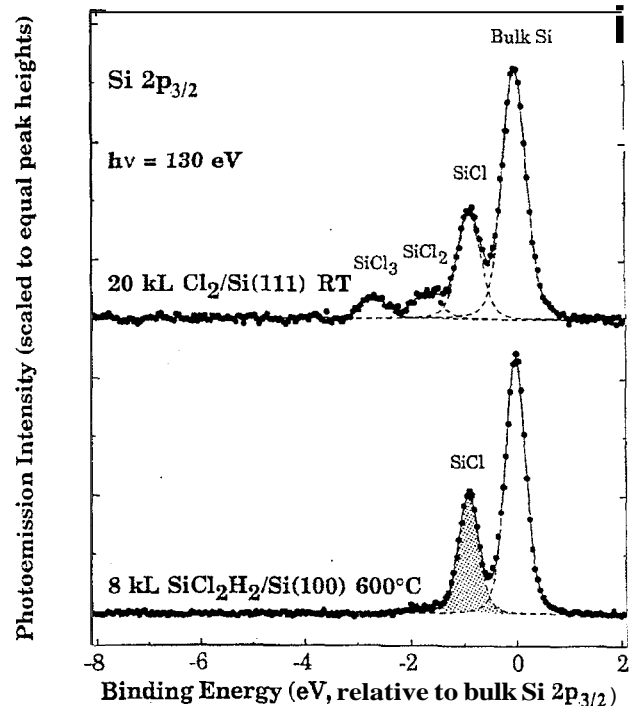

Figure 32: Study of surface reactions[46] occurring in atomic layer epitaxy (ALE) of Si on Si(100) via $SiCl_2H_2$. The surface is terminated by monochloride, indicating a pairing of the Si surface atoms. The truncated bulk structure would give dichloride.

chemical reaction in the second step. For Si deposition, a process with SiH_2CL_2 in the first step and H_2 in the second step has been suggested. In a naive picture one might expect the two hydrogens to be stripped in the adsorption process, and the remaining $SiCL_2$ species to be bonded to the two broken bonds per surface atom on the ideal Si(100) surface. The Si 2p spectrum in Fig. 32 (Ref.[46]), however, shows clearly that only a single Cl is bonded to the Si surface atoms. This can be explained by a dimerization of the Si surface atoms (similar to that on the clean Si(100)2×1 surface), which ties up one of the two broken bonds per surface atom, and saturates the other with Cl.

IV.3 Interfaces

One of the main reasons for the dominant role of Si technology in todays microelectronics industry is the high electrical quality of the SiO_2/Si interface. It has less than 10^{-5} electrically active defects per interface atom. Yet the actual structure of the interface remains controversial. This is in part due to the amorphous

nature of the oxide, which does not allow for a definitive interfare structure, only for a class of local bonding configurations. Looking at this interface with Si 2p core level spectroscopy in Fig. 27 (Ref.[39]) one can clearly distinguish all intermediate oxidation states of Si. Their distribution puts stringent constraints on the interface bond topology, and rules out a number of interface motlels. It is interesting to note that all the intermediate oxidation states are unstable in the bulk, e.g. Si^{2+} corresponding to SiO disproportionates into Si and SiO_2 upon heating. Thus it has become possible to freeze in an unstable bond configuration at the interface by offering Si bonds on one side and oxygen bonds from the other. A similar stabilization of an unusual oxidation state is observed for the $CaF_2/Si(111)$ interface.

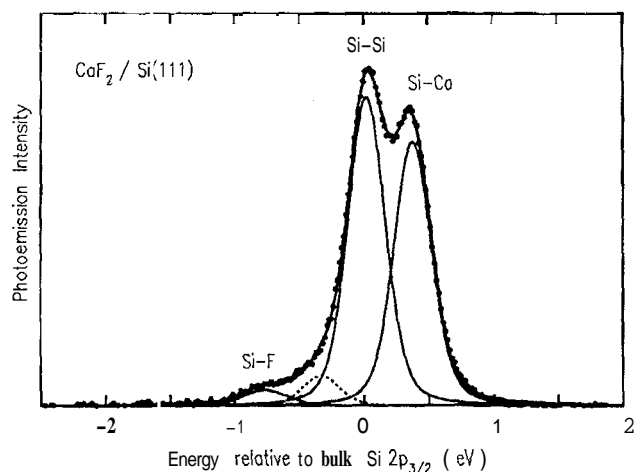Figure **33**: Bonding at the $CaF_2/Si(111)$ interface showing predominantly Si-Ca bonding across the interface[38,47].

The $CaF_2/Si(111)$ interface is easier to quantify than the SiO_2/Si since it is epitaxial. If this interface could be grown with the same defect level as SiO_2/Si it would makr a whole new class of three-dimensional device structiires feasible, from stacked CMOS to sophisticated, three-dimensional networks. The obvious question is: Does Si bond to Ca or to F at the interface. The Si 2p spectrum shows clearly that the majority of the Si atorns at the interface bonds to Ca for interfaces grown at high temperature (Fig. 33, Refs.[38,47]). However, theie is a small amount of Si-F bonding associated with defects. These defects would have to be brought down by several orders of magnitude to make this interface useful for devices. Structural models propose one F^- layer to be removed at the interface to enable Ca-Si bonding. The electron left by the F transforms Ca from the common 2+ to the unusual 1 + oxidation state. Thereby it obtains an unpaired 4s

electron, which can now pair up with the electron in the single broken bond of the Si(111) surface to form a bond across the interface. The corresponding bonding and antibonding valence orbitals have been seen by photoemission[48] inverse photoemission[49], and optical second harmonic generation[31]. The band gap of the interface is twice as large as that of Si, and five times smaller than in CaF_2, showing how unusual chemistry leads to dramatic changes in the electronic structure at interfaces.

IV.4 Element-Sensitive Microscopy

Core levels provide an identification of the elements and their oxidation states in a class of microscopies based on soft x-rays, e.g. using photoelectrons for imaging, or scanning a sample with a highly-focussed soft x-ray beam. The new generation of undulator-based synchrotron radiation sources with their extremely high brilliance is ideally-matched to such rnicroscopies. Here we just highlight some key aspects of this field.

It has long been a drawback of most microscopes that they were unable to identify various elements. For example, a scanning tunneling microscope can see atoms, but cannot identify them directly. Scanning Auger microscopy is one of the few exceptions. By using photoelectrons instead of Auger electrons for imaging one gains many orders of magnitude in the signal-to-background ratio. First, the efficiency for excitation is optimized by exciting core levels with nearly 100% efficiency at threshold, while the probability of exciting core levels by electrons is only 10^{-3} or less, particularly for deeper core levels. The remaining electrons create secondaries, which form a background under the Auger lines that is generally more intense than the signal, thus requiring exceptionally long integration times to improve statistical noise. This background is negligible with photon excitation, and the statistical noise is only determined by the Auger electron signal. As a consequence, it will be possible to perform the equivalent of scanning Auger microscopy with many orders of magnitude higher efficiency, allowing the study of radiation-sensitive materials, such as polymers and oxides. In addition, it will be possible to identify the chemical state of each element by its core level shift. There are two ways to select a specific element or oxidation state. One is to energy-analyze the core level photoelectrons, the other to tune into a particular absorption edge and use its fine structure to select the chemical state.

The applications that one can foresee include the analysis of microelectronic device structures and the structure of composite materials (e.g. different polymers and their cohesion). Other interesting fields are
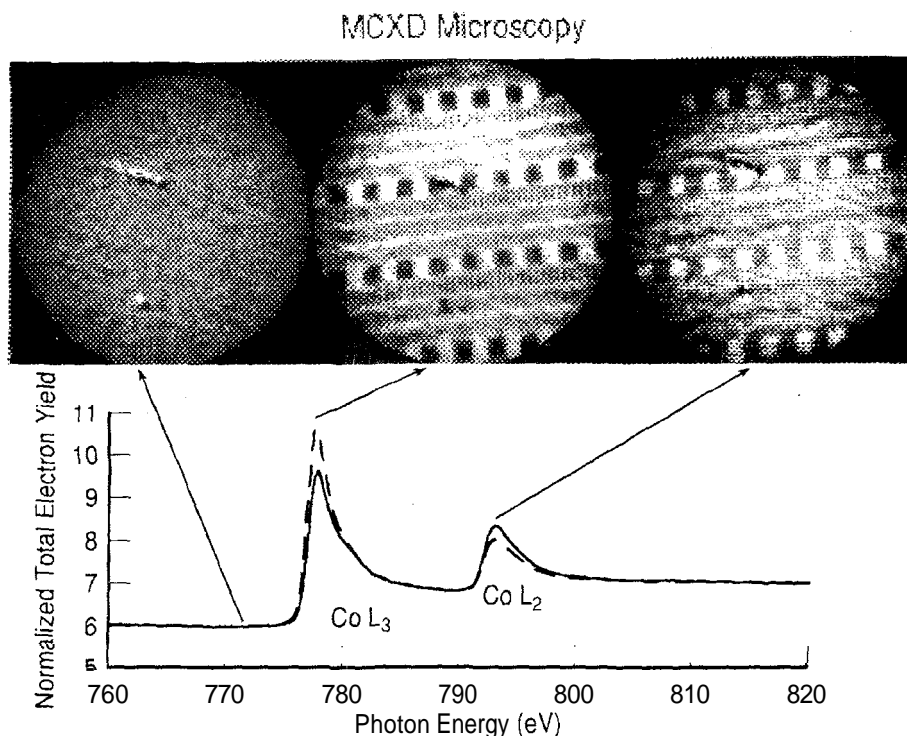
MCXD Microscopy

Figure 34: Images of magnetic domains[50] written onto a magnetic recording disk in a photoelectron microscope using circulady polarized soft x-rays. Magnetic circular dichroism leads to opposite magnetic contrast for the L_3 and L_2 absorption edges of Co.

segregation plienomena, nucleation and growth. The example in Fig. 34 (Ref.[50]) shows an image of data recorded on a magnetic disk. In this case the magnetic dichroism, i.e. a change in absorption from left- to right-handed circularly-polarized light, is used to display the orientation of the magnetic domains. Secondary photoelectrons are used for imaging, which give a signal proportional to the absorption coefficient. The element selectivity is very informative, since magnetic recording media are typically ternary compounds, e.g. CoPtCr for the case shown. By looking at the magnetic signal at different absorption edges one can select the magnetizãtion in different sub-lattices. The spatial resolution required for obtaining useful information from microelectronic devices is in the order of 0.1 μm. This is achievable with current imaging systems, either hy accelerating the photoelectrons to 20 keV and magnifying in a microscope column, or by focussing the soft x-rays with zone plates or mirrors.

References

1. *Photoemission* in *Solids I and II*, ed. by M. Cardona and L. Ley (Springer Topics in Applied Physics, Berlin, 1978, 1979). Vol. 26, 27.

2. F. J. Himpsel and N. V. Smith, Physics Today, 38, Nr.12, 60 (1985).

3. For reviews on angle-resolved photoemission see E. W. Plummer and W. Eberhardt, Adv. Chem. Phys. 49, 533 (1982); F. J. Himpsel, Adv. Phys. 32, 1 (1983).

4. Y. Petroff, High resolution photoemission of 16. D and 2D systems, Braz. J. Phys., to be published.

5. C. E. Kuyatt and J. A. Simpson, Rev. Sci. Instrum. 38, 103 (1967); S. D. Kevan, Rev. Sci. Instrum. 54, 1441 (1983); U. Gelius, B. Wannaberg, P. Baltzer, H. Fellner-Feldegg, G. Carlsson, C.-G. Johansson, J. Larsson, P. Munger and G. Vegerfors, J. Electron. Spec. and Rel. Phenom. 52, 747 (1990).

6. H. A. Engelhardt, W. Rack and D. Menzel, Rev. Sci. Instrum. 52, 835 (1981); R. G. Smeenk, R. M. Tromp, H. H. Kestern, A. J. H. Boerboom and F. W. Saris, Nucl. Instrum. Methods 195, 581 (1982); G. J. A. Hellings, H. Ottevanger, C. L. C. M. Knibbeler, J. van Engelshoven and H. H. Brongersma, J. Elec. Spec. and Rel. Phenom., 49, 459 (1989); R. Leckey, J. D. Riley and A. Stampfl, J. Elec. Spec. and Rel. Phenom. 52, 855 (1990).

7. D. E. Eastman, J. J. Donelon, N. C. Hien, and F. J. Himpsel, Nucl. Instrum Methods 172, 327 (1980); D. Rieger, V. Saile, R.-D. Schnell and W. Steinmann, Nucl. Instrum. Methods, 208, 777 (1983); R. L. Kurtz, S. W. Robey, L. T. Hudson, R. V. Smiglys, and R. L. Stockbauer, Nucl. Instrum. Methods A319, 257 (1992).

8. H. Dainon, Y. Tezuka, A. Otaka, N. Kanada, S. K. Lce S. Ino, H. Namba and H. Kuroda, Surf. Sci. 242, 288 (1991).

9. J. J. Barton, Rev. Sci. Instrum., submitted.

10. J. Unguris, D. T. Pierce, and R. J. Celotta, Rev. Sci. Instrum. 57, 1314 (1986).

11. R. A. Bartynski, E. Jensen and S. L. Hulbert, Physica Scripta T41 168 (1992).

12. F. J. Himpsel, Comments Cond. Mat. Phys. 12, 199 (1936).

13. J. E. Ortega and F. J. Himpsel, Phys. Rev. B47, 2130 (1993); M. S. Hybertsen and S. G. Louie, Phys. Rev. B34, 5390 (1986).

14. E. Jensen and E. W. Plummer, Phys. Rev. Lett. 55, 1912 (1985); J. E. Northrup, M. S. Hybertsen and S. G. Louie, Phys. Rev. Lett. 59, 819 (1987); In-Whan Lyo and E. W. Plummer, Phys. Rev. Lett. 60, 1558 (1988).

15. F. J. Himpsel, L. J. Terminello, D. A. Lapiano-Smith, E. A. Eklund, and J. J. Barton, Phys. Rev. Lett. 68, 3611 (1992).

16. L. E. Klebanoff, R. H. Victora, L. M. Falicov, and D. A. Shirley, Phys. Rev. B32, 1997 (1985); R. Richter, J. G. Gay and J. R. Smith, Phys. Rev. Lett. 54, 2704 (1985); C. L. Fu, A. J. Freeman, and T. Oguchi, Phys. Rev. Lett. 54, 2700 (1985); S. Blügel, B. Drittler, R. Zeller, and P. H. Dederichs, Appl. Phys. A49, 547 (1989).

17. S. Bade and E. R. Moog, J. Appl. Pliys. 61, 3729 (1987); W. Dürr, M. Taborelli, O. Paul, R. Germar, W. Gudat, D. Pescia, and M. Landolt, Phys. Rev. Lett. 62, 206 (1989); W. Heinen, C. Carbone, T. Kachel, and W. Gudat, J. Elect. Spect. and Rel. Phenom., 51, 701 (1990); F. J. Himpsel, Phys. Rev. B44, 5966 (1991).

18. E. Kisker, A. Schroder, M. Campagna, and W. Gudat, Phys. Rev. Lett. 52, 2285 (1984) and Phys. Rev. B31, 329 (1985).

19. A. Santoni and F. J. Himpsel, Phys. Rev. B43, 1305 (1931).

20. F. J. Himpsel, Phys. Rev. Lett. 67, 2363 (1991); F. J. Himpsel, J. Magn. Magn. Mat. 102, 261 (1991); I. Turek, Ch. Becker and J. Hafner, J. Phys. Condens. Matter 4, 7257 (1992).

21. R. A. Pollak, D. E. Eastman, F. J. Himpsel, P. Heimann, and B. Reihl, Phys. Rev. B24, 7435 (1981); N. V. Smith, S. D. Kevan and F. J. DiSalvo, Sol. State Phys. 18, 3175 (1985); B. Dardel, M. Grioni, D. Malterre, P. Weibel, and Y. Baer, Phys. Rev. B45, 1462 (1992).

22. Y. Hwu, L. Lozzi, M. Marsi, S. La Rosa, M. Winokur, P. Davis, and M. Onellion, Phys. Rev. Lett. 67, 2573 (1991).

23. S. D. Kevan, Physica Scripta, T31, 32 (1990).

24. A. Santoni, L. J. Terminello, F. J. Himpsel, and T. Takahashi, Appl. Phys. A52, 299 (1991).

25. F. J. Himpsel, Surface Science Reports 12, 1 (1990); E. Kaxiras, K. C. Pandley, F. J. Himpsel and R. M. Tromp, Phys. Rev. B41, 1262 (1990).

26. P. J. Feibelman, D. R. Hamann, and F. J. Himpsel, Phys. Rev. B22, 1734 (1980).

27. D. A. Lapiano-Smith, F. J. Himpsel, and L. J. Terminello, J. Appl. Phys., submitted.

28. W. D. Grobman and E. E. Koch, Chapter 5 in *Photoemission in Solids II,* ed. by L. Ley and M. Cardona (Springer Topics in Applied Physics, Berlin, 1979), Vol. 27, 261, see in particular Fig. 5.2.

29. J. Stohr and R. Jaeger, Phys. Rev. B26, 4111 (1982).

30. F. J. Himpsel, G. V. Chandrashekhar, A.B. Mc Lean, and M.W. Shafer, Phys. Rev. B38, 11946 (1988).

31. T. F. Heinz, F. J. Himpsel, E. Palange and E. Burstein, Phys. Rev. Lett. 63, 644 (1989).

32. A. B. McLean and F. J. Himpsel, Phys. Rev. B40, 8425 (1989); F.J. Himpsel, W. Drube, A. B. McLean, and A. Santoni, Appl. Surf. Sci. 56-58, 160 (1992).

33. L. Falicov, Braz. J. Phys. 23 (1993).

34. W. P. Pratt, Jr., S.-F. Lee, J. M. Slaughter, R. Loloee, P. A. Schroeder, and J. Bass, Phys. Rev. Lett. 66, 3060 (1991); S. F. Lee, W. P. Pratt, Jr., R. Loloee, P. A. Schroeder, and J. Bass, Phys. Rev. B46, 548 (1992).

35. H. Eckardt, L. Fritsche, and J. Noffke, J. Phys. F14, 97 (1984); H. Erschbaumer, A. J. Freeman, C. L. Fu, and R. Podloucky, Surf. Sci. 243, 317 (1991).

36. J. E. Ortega and F. J. Himpsel, Phys. Rev. Lett. 69, 844 (1992); J. E. Ortega, F.J. Himpsel, G. J. Mankey, and R.F. Willis, Phys. Rev. B47, 1540 (1993).

37. L. J. Terminello, D. K. Shuh, F. J. Himpsel, D. A. Lapiano-Smith, J. Stohr, D. S. Bethune, and G. Meijer, Chem. Phys. Lett. 182, 491 (1991).

38. F. J. Himpsel, B. S. Meyerson, F. R. Mc Feely, J. F. Morar, A. Taleb-lbrahimi, and J. A. Yarmoff, Core Level Spectroscopy at Silicon Surfaces and

Interfaces. Proceedings of the Enrico Fermi School on *Photoemission and Absorption Spectroscopy of Solids and Interfaces with Synchrotron Radiation,* ed by M. Campagna and R. Rosei (North Holland, Amsterdam, 1990) p. 203.

39. F. J. Himpsel, F. R. Mc Feely, A. Taleb-Ibiahimi, J. A. Yarmoff, and G. Hollinger, Phys. Rev. B38, 6084 (1982).

40. Additional data for Yb and Al are included from C. Wigren, PhD Thesis, University of Lund, Sweden (1992).

41. F. J. Hirnpsel, Appl. Phys. A38, 205 (1985); J. F. Morar, F. J. Himpsel, G. Hollinger, J. L. Jordan, G. Hughes, and F. R. McFeely, Phys. Rev. B33, 1340 (1986); F. R. McFeely, J. F. Morar, N. D. Shinn, G. Landgren, and F.J. Himpsel, Phys. Rev. B30, 764 (1984); F. R. McFeely, J. F. Morar, and F. J. Himpsel, Surf. Sci. 165, 277 (1986).

42. E. Rotenberg and M. Olmstead, Phys. Rev. B46, 12284 (1992).

43. J. Bozek, G. M. Bancroft, J. N. Cutler, and K. H. Tan, Phys. Rev. Lett. 65, 2757 (1990); D. G. J. Sutherland, G. M. Bancroft, and K. H. Tan, Surf. Sci. Lett. 262, L96 (1992).

44. B. S. Meyerson, F. J. Hirnpsel, and K. J. Uram, Appl. Phys. Lett. 57, 1034 (1990).

45. G. W. Trucks, K. Raghavachari, G. S. Higashi and Y. J. Chabal, Phys. Rev. Lett. 65, 504 (1990).

46. J. A. Yarmoff, D. K. Shuh, T. D. Durbin, C. W. Lo, D. A. Lapiano-Smith, F. R. McFeely, and F. J. Himpsel, J. Vac. Sci Technol. A10, 2303 (1992).

47. D. Rieger, F. J. Himpsel, U. O. Karlsson, F. R. Mc Feely, J. F. Morar, and J. A. Yarmoff, Phys. Rev. B34, 7295 (1986); M. A. Olmstead, R. I. G. Uhrberg, R. D. Bringans and R. Z. Bachrach, Phys. Rev. B35, 7526 (1986).

48. A. B. McLean and F. J. Himpsel, Phys. Rev. **39,** 1457 (1989).

49. S. Bouzidi, F. Coletti, J. M. Debever, J. Longueville, and P. A. Thiry, Appl. Surf. Sci. 56, 821 (1992).

50. J. Stohr, Y. Wu, B. D. Hermsmeier, M. G. Samant, and G. R. Harp, submitted to Science.